Research Square

Preprints are preliminary reports that have not undergone peer review.
They should not be considered conclusive, used to inform clinical practice,
or referenced by the media as validated information.

Disentangling postseismic deformation from noisy GNSS data using vbICA approach: Application to the 2021 Mw7.4 Maduo Earthquake, Tibetan Plateau

Zhijun Liu

1021231016@tju.edu.cn

Tianjin University https://orcid.org/0009-0001-1051-1862

Qiang Qiu

South China Sea Institute of Oceanology Chinese Academy of Sciences

Jing Liu-Zeng

Tianjin University School of Earth System Science: Tianjin University Institute of Surface-Earth System Science

Yunfeng Tian

Ministry of Emergency Management of the People's Republic of China

Bin Zhao

Institute of Seismology China Earthquake Administration

Peng Wang

China Earthquake Administration Institute of Geology

Wenqian Yao

Tianjin University School of Earth System Science: Tianjin University Institute of Surface-Earth System Science

Wenxin Wang

Tianjin University School of Earth System Science: Tianjin University Institute of Surface-Earth System Science

Longfei Han

China Earthquake Administration The First Monitoring and Application Center

Yanxiu Shao

Tianjin University School of Earth System Science: Tianjin University Institute of Surface-Earth System Science

Research Article

Keywords:

Posted Date: October 26th, 2026

DOI: https://doi.org/10.21203/rs.3.rs-10721869/v1

License: This work is licensed under a Creative Commons Attribution 4.0 International License.
Read Full License

Title: Disentangling postseismic deformation from noisy GNSS data using vbICA approach: Application to the 2021 Mw7.4 Maduo Earthquake, Tibetan Plateau

Author #1: Zhijun Liu, Institute of Surface-Earth System Science, School of Earth System Science, Tianjin University, Tianjin, China, 1021231016@tju.edu.cn

Author #2: Qiang Qiu, State Key Laboratory of Tropical Oceanography, South China Sea Institute of Oceanology, Chinese Academy of Sciences, Guangzhou, China, qiu.qiang@scsio.ac.cn

Author #3: Jing Liu-Zeng, Institute of Surface-Earth System Science, School of Earth System Science, Tianjin University, Tianjin, China, liu_zeng@tju.edu.cn

Author #4: Yunfeng Tian, National Institute of Natural Hazards, Ministry of Emergency Management of China, Beijing, China, tianyf@gmail.com

Author #5: Bin Zhao, Key Laboratory of Earthquake Geodesy, Institute of Seismology, China Earthquake Administration, Wuhan, China, zhaobin@cgps.ac.cn

Author #6: Peng Wang, State Key Laboratory of Earthquake Dynamics, Institute of Geology, China Earthquake Administration, Beijing, China, wpeng0909@126.com

Author #7: Wenqian Yao, Institute of Surface-Earth System Science, School of Earth System Science, Tianjin University, Tianjin, China, wenqian_yao@tju.edu.cn

Author #8: Yanxiu Shao, Institute of Surface-Earth System Science, School of Earth System Science, Tianjin University, Tianjin, China, shaoyx@tju.edu.cn

Author #9: Wenxin Wang, Institute of Surface-Earth System Science, School of Earth System Science, Tianjin University, Tianjin, China, wenxinwwx_1995@tju.edu.cn

Author #10: Longfei Han, The First Monitoring and Application Center, China Earthquake Administration, Tianjin, China, hanlongfei_2019@tju.edu.cn

Indicate the corresponding author

Corresponding author: Jing Liu-Zeng

Email: liu_zeng@tju.edu.cn

(go to new page)

Abstract

Near-rupture GNSS stations on the Tibetan Plateau are commonly installed after large earthquakes because continuous pre-earthquake coverage is sparse. The absence of pre-seismic records at these stations challenges the separation of complex and entangled postseismic decay deformation from e.g., background linear trends, regional seasonal variations and other noises. Here, we apply the variational Bayesian independent component analysis (vbICA) approach to postseismic GNSS (19 continuous GNSS stations installed before and 13 installed after the earthquake) time series following the 2021 Mw 7.4 Maduo earthquake. To do so, we first process the 19 GNSS time series by identifying the coseismic, non-tectonic offsets and estimate the long-term linear trend, and then removed them both. We then apply vbICA to disentangle the residual time series to obtain postseismic transient and regional seasonal components from other noises. We further use the Kriging method to interpolate the linear trend and seasonal components estimated from the 19 continuous stations to the 13 stations installed after the earthquake, and remove them from the time series. Finally, we apply vbICA to all the residual time series to extract the postseismic deformation pattern. To maximize the postseismic deformation extraction, we apply vbICA to horizontal and vertical components separately for the strike-slip Maduo earthquake, with horizontal movement dominating the postseismic deformation field. Our results show that the horizontal component of postseismic deformation illuminates exponential shape transient with rapid decaying rate within a year and then progressively to a consistent rate during the observational time period; in contrast, the vertical component does not show such a clear transient feature. Our results underscore that the vbICA approach disentangles postseismic deformation pattern from an observational work, potentially offering an improved solution for

studying postseismic relaxation processes that are happening in both continents and subduction zones.

Keywords

GNSS time series; postseismic deformation; variational Bayesian independent component analysis; seasonal displacement; 2021 Mw7.4 Maduo earthquake; Tibetan Plateau

1. Introduction

The convergence between the Indian and Eurasian plates has formed the Tibetan Plateau as a typical intracontinental collisional orogen, where large-scale uplift and crustal shortening record the long-term tectonic consequences of Cenozoic continental collision (Molnar & Tapponnier, 1975; Yin & Harrison, 2000; Tapponnier et al., 2001). Under continued convergence and intracontinental tectonic adjustment, a series of major active faults have developed within and around the plateau, closely associated with the present-day distribution of large earthquakes and regional strain field (Taylor & Yin, 2009). GNSS observations can provide essential constraints for understanding kinematic deformation of the Tibetan Plateau and the physical properties of the lithosphere (Bürgmann & Thatcher, 2013; Bock & Melgar, 2016; Wang & Shen, 2020; Wang et al., 2021). Latest GNSS velocity fields showed that present-day crustal motion across the Tibetan Plateau is characterized by spatially heterogeneous deformation involving block motion and crustal shortening (e.g., Zhang et al., 2004; Gan et al., 2007; Wang & Shen, 2020). In the case of large earthquakes, GNSS observations offered direct constraints for

characterizing fault slips and the viscoelastic response of the lower crust and upper mantle, for example, the 2001 Kokoxili Mw 7.8 earthquake (Ryder et al., 2011), the 2008 Mw 7.9 earthquake (Wang et al., 2021), and the 2015 Gorkha (Nepal) Mw7.8 earthquake (Liu-Zeng et al., 2020).

GNSS coverage is sparse across the Tibetan Plateau and stations close to earthquake ruptures were very limited. New GNSS stations may be deployed after an earthquake to improve the spatial coverage for constraining detailed characterization of early postseismic displacement evolution (Liu-Zeng et al., 2020), but data records usually begin several days to weeks after the event. Postseismic GNSS coordinate time series may contain seasonal displacements, coordinate offsets, and colored noise that overlap with postseismic decay deformation and complicate identification of the target signal (Dong et al., 2002; Williams et al., 2004). The lack of pre-seismic data at newly deployed stations makes it elusive to accurately isolate transient post-seismic deformation from background linear trends and seasonal variations (Liu-Zeng et al., 2020). Some studies use conventional single-station trajectory models that jointly fit long-term linear trends, coordinate offsets, annual and semiannual harmonic terms, and empirical exponential or logarithmic functions describing postseismic decay (Nield et al., 2023). Singular spectrum analysis, Kalman filtering, and wavelet decomposition have also been developed to model seasonal signals with interannual variations in amplitude and phase (Klos et al., 2018). Fixed harmonic terms assume stable seasonal amplitudes and phases, whereas background trends and seasonal terms cannot be independently estimated from the postseismic record alone at stations without pre-seismic observations; the precision of time-varying seasonal estimates is further affected by observation span and time-

correlated noise (Klos et al., 2018; Liu-Zeng et al., 2020). Identifying common temporal variations and their spatial patterns in multi-station GNSS time series, isolating the seasonal components, and using them to reconstruct seasonal displacements and correct postseismic records at stations deployed after an earthquake can reduce seasonal contamination in the extraction of postseismic decay signals (Gualandi et al., 2016; Liu-Zeng et al., 2020).

The 2021 Mw 7.4 Maduo earthquake ruptured the Jiangcuo Fault within the Bayan Har block in the northeast Tibetan Plateau, producing a ~158-km-long surface rupture and complex rupture behavior involving branching, propagation, and termination (Liu-Zeng et al., 2022, 2024; Yao et al., 2024). Existing InSAR-based and multi-source studies have constrained the coseismic rupture process, the three-dimensional coseismic displacement field, and the distribution of early postseismic deformation, yielding a well-resolved spatial deformation pattern for the Maduo region (Jin & Fialko, 2021; Xiong et al., 2022; Jin et al., 2023; Xu et al., 2023; Tian et al., 2024; Li et al., 2025). Continuous GNSS time series, in turn, record the temporal evolution of three-dimensional station displacements, making the reliable extraction of postseismic transients from these records essential for characterizing postseismic deformation.

To accurately extract postseismic decay signals following the 2021 Maduo earthquake, we combined data from long-running stations with pre-seismic records and stations installed after the earthquake. We first introduce the GNSS data set, data processing, time series modeling, and a signal-separation strategy based on variational Bayesian independent component analysis. We then apply this method to position time series from the long-running stations to extract regional seasonal components and correct

post-seismic position time series. Postseismic decay signals are then extracted from the seasonally corrected three-dimensional GNSS time series. The stability of the extracted signals is evaluated by comparing results obtained using different decomposition schemes and by examining their agreement with previously published deformation results. Finally, we discuss the applicability and limitations of this processing approach for postseismic GNSS time-series analysis on the Tibetan Plateau.

To accurately extract postseismic decay signals following the 2021 Maduo earthquake, we combined data from continuous GNSS stations installed before and after the earthquake. We first introduce the GNSS data set, data processing and a signal-separation strategy based on variational Bayesian independent component analysis (vbICA). We then apply this method separately to the preprocessed east, north, and vertical position time series spanning the pre-earthquake and postseismic intervals at the continuous stations installed before the earthquake to identify and extract regional seasonal components, which are used to correct the corresponding postseismic GNSS time series. We subsequently apply vbICA separately to the seasonally corrected east, north, and vertical GNSS time series to extract postseismic decay deformation. The stability of the extracted signals is evaluated by comparing the separately obtained east, north, and vertical results with those from the joint three-component decomposition and by examining their agreement with previously published deformation results. Finally, we discuss the applicability and limitations of this processing approach for postseismic GNSS time-series analysis on the Tibetan Plateau.

2. Data and signal extraction method

2.1 GNSS data and processing

Before the 2021 Mw 7.4 Maduo earthquake, continuous GNSS coverage around the Jiangcuo Fault and its surrounding region was insufficient to fully capture the spatial variability of three-dimensional postseismic displacement, particularly in the near field. To improve continuous displacement observations in the rupture region, we installed 12 continuous GNSS stations within approximately 40 km of the coseismic surface rupture and one far-field station, QSHZ, approximately 90 km south of the surface rupture. The new stations were installed progressively between two weeks and one month after the mainshock. Six stations are installed on bedrock, whereas seven are installed on four-legged braced monuments. The available observations from these stations collectively span approximately two years of the postseismic period, although observation spans and data continuity vary among stations; subsequent time-series analysis uses the available records at each station. In addition, we collected observations from 19 continuous GNSS stations within approximately 500 km of the epicenter (Fig. 1), including 11 stations from the Crustal Movement Observation Network of China and 8 stations from the Qinghai-CORS network. Their records span 1 January 2017 to 1 June 2023. Several Qinghai-CORS stations contain data gaps over limited intervals; however, the available records cover the periods required to characterize background variations before the earthquake and postseismic deformation.

Fig. 1. Tectonic setting of the 2021 Mw 7.4 Maduo earthquake and distribution of

continuous GNSS stations. Red and black triangles denote stations installed before and after the earthquake, respectively. Circles show aftershocks, coloured by focal depth. The beachball denotes the focal mechanism, and the star marks the epicentre. The red trace shows the mapped coseismic surface rupture, and grey lines denote major active faults. The inset shows major active faults and schematic block rotations across the Tibetan Plateau, modified after Tapponnier et al. (2001) and Avouac and Tapponnier (1993). ATF, Altyn Tagh Fault; HF, Haiyuan Fault; KF, Kunlun Fault; XSHF, Xianshuihe Fault.

We processed raw GNSS observations using GAMIT/GLOBK 10.71 (Herring et al., 2018). Each daily GAMIT solution jointly included the regional stations and 21 IGS stations (Fig. S1) distributed around the study area. Ionosphere-free, double-differenced carrier-phase observations were used to estimate station coordinates, satellite orbital parameters, zenith tropospheric delays, horizontal gradients, and phase ambiguities, yielding daily loosely constrained regional solutions and their associated covariance matrices. We used VMF1 mapping functions for the hydrostatic and wet tropospheric delays, estimated zenith delays at 2-h intervals and two horizontal-gradient parameters per day, and applied solid Earth tide, frequency-dependent tide, and pole-tide corrections in accordance with the IERS 2010 conventions (Böhm et al., 2006; Petit and Luzum, 2010). Ocean-tide loading was corrected using the FES2004 model (Lyard et al., 2006). After combining the daily regional solutions in GLOBK, GLORG used the a priori coordinates and velocities of the 21 IGS stations from the IGb14 realization to stabilize the solutions in the ITRF2014 reference frame (Altamimi et al., 2016; Rebischung et al., 2016). Finally, we transformed the resulting geocentric coordinates into local east, north,

and up components to obtain daily GNSS position time series for subsequent preprocessing and signal separation.

Prior to extracting postseismic deformation, the raw GNSS coordinate time series were preprocessed to remove coordinate offsets and long-term linear trend. For stations installed before the earthquake, the most prominent offsets are coseismic displacements of the 2021 Maduo earthquake. They were estimated from the difference between the mean positions over the three days immediately before and after the earthquake. Coordinate offsets can also be caused by non-tectonic factors, such as station maintenance, equipment changes, and antenna-height changes. Such offsets were estimated according to the station logs and antenna-height records in the RINEX observation files. We estimated linear velocities for the pre-seismic stations using four years of pre-earthquake observations with Hector software (Bos et al., 2013). We adopted a combination of power-law and white noise models (PLWN) to account for temporally correlated noise in the velocity estimates and their associated uncertainties (Stamps & Kreemer, 2024). The velocity estimates from the 19 pre-seismic stations define the background velocity field. We used Kriging to interpolate this field to the 13 stations installed after the earthquake (Fig. 2; Cressie, 1993; Gualandi et al., 2017). We removed all coordinate offsets and the long-term linear trend from each component of the station position time series. The resulting preprocessed east, north, and vertical GNSS position time series were used separately as input for subsequent postseismic deformation separation (Fig. S2).

Fig. 2. Long-term GNSS velocity field and Kriging-interpolated background velocities used for time-series detrending. (a) Horizontal velocity field. (b) Vertical velocity field.

Red vectors denote velocities estimated at continuous GNSS stations installed before the earthquake, whereas black vectors denote background velocities interpolated by Kriging at stations installed after the earthquake. Red and black triangles identify the corresponding station groups. Vector scales are shown in the lower-left corner of each panel. In panel (b), upward and downward arrows indicate positive and negative vertical velocities, respectively.

2.2 vbICA-based post-seismic signal extraction

We apply variational Bayesian independent component analysis (vbICA; Choudrey, 2002) to separate the components associated with postseismic decay deformation from the preprocessed GNSS time series. vbICA is a blind source separation method that represents the GNSS observations as a linear combination of statistically independent components without prescribing the temporal functions or spatial patterns of the underlying signals. Each independent component is characterized by a temporal function, a spatial response, and an associated weight, allowing components with distinct spatiotemporal characteristics to be isolated from the position time series of multi-station GNSS observations. In contrast to principal component analysis (PCA), which is based on variance maximization and orthogonal decomposition, independent component analysis (ICA) emphasizes statistical independence among source signals. In the variational Bayesian framework, Automatic Relevance Determination (ARD) provides a statistical constraint on the number of retained components, but the final selection also requires consideration of the temporal functions, spatial responses, and physical interpretability of the components (Choudrey, 2002; Gualandi et al., 2016, 2017). Because linear trends and coseismic offsets can influence the ARD constraint and complicate component interpretation, we use the preprocessed time series described in Section 2.1 as input for signal separation.

For each east, north, and vertical analysis, we arrange the preprocessed GNSS position time series from individual stations into an observation matrix and decompose it using the following linear mixing model:

$$\mathrm{X}_{M\times T} \approx \mathrm{U}_{M\times R}\mathrm{S}_{R\times R}V^{T}_{R\times T}$$

where X is an $M \times T$ matrix containing the GNSS displacement time series, M is the number of input station time series, T is the number of observation epochs, and R is the number of retained independent components. Matrix U represents the spatial response of each independent component at the stations for the analysed coordinate component, V^T contains the corresponding temporal functions, and S is a diagonal weight matrix that quantifies the contribution of each independent component to the reconstructed displacement time series. The temporal functions and spatial responses are dimensionless, whereas the weights are expressed in units of displacement. For the joint three-component comparison, the east, north, and vertical time series are stacked as separate input series in the same formulation. This formulation reconstructs the displacement time series at each station for a given coordinate component from a finite number of independent components, their temporal functions, spatial responses, and weights.

Before extracting postseismic decay deformation, we corrected the east, north, and vertical GNSS position time series separately for regional seasonal variations. Seasonal displacement is one of the major non-tectonic components in GNSS position time series. It commonly appears as spatially coherent periodic variations, although its amplitude, phase, and spatial response may vary with environmental conditions, surface-loading processes, and station location (Dong et al., 2002; Larochelle et al., 2018; Yan et al., 2019). Uncorrected seasonal variations can affect the identification of postseismic decay deformation. This effect is particularly pronounced in the vertical component, which is more strongly affected by surface loading and generally has larger observational uncertainties and stronger noise (Fu and Freymueller, 2012; Santamaría-Gómez et al., 2011). Conventional single-station trajectory models commonly represent seasonal displacements using prescribed annual and semiannual terms; however, such parameterizations may not fully capture interannual variations and can become less stable for short observation records (Bevis and Brown, 2014; Bos et al., 2013; Kłos et al., 2018).

Although vbICA can in principle separate seasonal and postseismic components in a single decomposition when their temporal functions and spatial responses are sufficiently distinct and the postseismic signal is strong relative to seasonal variations and residual noise, these conditions are more difficult to satisfy at stations installed after the earthquake. Their available postseismic records are relatively short and contain data gaps

at some sites, while seasonal variations and postseismic decay deformation overlap within the same observation interval. In contrast, the pre-earthquake portions of the preprocessed time series from the 19 continuous stations installed before the earthquake contain repeated seasonal cycles without postseismic decay deformation associated with the Maduo earthquake. These records provide more stable constraints on regional common seasonal components and their spatial responses. We use the identified components to reconstruct the postseismic seasonal displacement time series at all stations, including those installed after the earthquake, and subtract the reconstructed seasonal time series from the corresponding postseismic GNSS position time series to reduce seasonal contamination in the subsequent extraction of postseismic decay deformation (Gualandi et al., 2017; Liu-Zeng et al., 2020).

We applied vbICA separately to the preprocessed east, north, and vertical GNSS position time series during the pre-earthquake interval at the 19 continuous GNSS stations to identify regional common components. We used the ARD curves and explained variance as initial statistical guidance for selecting the retained independent components, and we examined their temporal functions and spatial responses to characterize the separated signals. We identified the principal seasonal components from their spectral characteristics, temporal evolution, and spatial responses. Using a 365-day stacking procedure, we extended the temporal functions of the selected seasonal components to the two-year postseismic interval (Gualandi et al., 2017). For the 19 continuous stations, we directly reconstructed the postseismic seasonal displacement time series from the extended temporal functions, spatial responses, and weights of the selected components. For stations installed after the earthquake, we first interpolated the spatial responses of the selected seasonal components to the station locations using Kriging (Cressie, 1993) and then combined them with the corresponding extended temporal functions and weights to reconstruct the postseismic seasonal displacement time series. We subtracted the reconstructed seasonal time series from the preprocessed postseismic east, north, and vertical GNSS position time series at all stations to obtain seasonally corrected time series for subsequent postseismic deformation extraction.

We then applied vbICA separately to the seasonally corrected east, north, and vertical GNSS position time series from all 32 stations to extract postseismic decay deformation associated with the 2021 Mw 7.4 Maduo earthquake. The analysis window for each directional decomposition extended from approximately one month before the earthquake to 23 May 2023. The short pre-earthquake segment provided a temporal reference for evaluating whether the temporal functions changed at the earthquake epoch.

For the present data set, we selected the duration of this segment by considering the length and completeness of the available postseismic records. Because stations installed after the earthquake have no observations before the earthquake, extending this segment would increase the proportion of missing entries in the input matrix for each directional analysis. We did not identify components associated with postseismic deformation from the ARD results alone. Instead, we jointly evaluated their temporal functions, spatial responses, and reconstructed station time series, including whether the temporal functions showed a post-earthquake decay pattern, whether the spatial responses were compatible with deformation in the epicentral and coseismic rupture zones, and whether the reconstructed time series captured the principal postseismic changes at individual stations. We used the selected components to reconstruct the east, north, and vertical postseismic deformation time series separately.

3. Results

3.1 Identification and correction of regional seasonal components

Separate vbICA decompositions of the preprocessed east, north, and vertical GNSS position time series during the pre-earthquake interval at the 19 continuous GNSS stations retained three, two, and two independent components, respectively, based on the ARD curves and cumulative explained variance (Figs. S3, S5, and S7). The temporal functions and spatial responses of the retained components are shown in Figs. 3-5. In each directional decomposition, the temporal functions and spatial responses are dimensionless, whereas the value denoted by S is the component-specific scaling factor used to reconstruct station displacement time series and is expressed in millimetres.

The east-component decomposition identified IC3 as the principal seasonal component. Its temporal function exhibits recurrent annual behavior during the pre-earthquake interval and the strongest spectral power near 1 yr−1 among the retained east-component ICs (Fig. S4). The two retained north-component ICs both show periodic temporal variations and discernible annual spectral power (Figs. 4 and S6). In the vertical component, the two retained ICs exhibit repeated periodic variations, with spatial responses that differ among stations but retain a coherent regional pattern (Fig. 5; Fig. S8). The temporal functions of these selected components were extended to the postseismic interval using the 365-day stacking procedure. Components without

sustained periodic temporal behavior or with spatial responses dominated by local differences were not included in the seasonal reconstruction.

Fig. 3. Separate vbICA decomposition of the preprocessed east-component GNSS position time series during the pre-earthquake interval. Panels (a)-(c) show the spatial responses and temporal functions of IC1-IC3, respectively, obtained from the 19 continuous GNSS stations. Open circles denote stations used in the initial decomposition, and blue triangles denote stations installed after the earthquake, where the spatial responses were obtained by Kriging interpolation. Black and cyan segments show the temporal functions estimated during the pre-earthquake interval and their 365-day-stacked extensions over the postseismic interval, respectively. The red star marks the epicentre of the 2021 Mw 7.4 Maduo earthquake. Red dashed lines denote the mapped coseismic surface rupture in the maps and the earthquake epoch in the temporal-function plots. Arrows show east-component spatial responses, and the reference vector is given in each map. S is the component-specific scaling factor used to reconstruct station displacement time series and is expressed in millimetres.

Fig. 4. Separate vbICA decomposition of the preprocessed north-component GNSS position time series during the pre-earthquake interval. Panels (a) and (b) show IC1 and IC2, respectively. The spatial responses and temporal functions are arranged as in Fig. 3; arrows show north-component spatial responses. All symbols and line styles are defined in Fig. 3.

Fig. 5. Separate vbICA decomposition of the preprocessed vertical-component GNSS position time series during the pre-earthquake interval. Panels (a) and (b) show IC1 and IC2, respectively. The spatial responses and temporal functions are arranged as in Fig. 3; upward and downward arrows show positive and negative vertical spatial responses. All symbols and line styles are defined in Fig. 3.

We reconstructed the postseismic seasonal displacement time series separately for the east, north, and vertical components at all stations using the selected seasonal ICs. For the 19 continuous stations, the reconstruction directly combines the extended temporal functions with the corresponding spatial responses and scaling factors. For stations installed after the earthquake, we interpolated the spatial responses of the selected seasonal components to the station locations using Kriging before reconstruction. The

cyan segments in Figs. 3-5 show the extended seasonal temporal functions, and the responses shown at stations installed after the earthquake represent the interpolated spatial patterns used for reconstruction. Subtracting the reconstructed seasonal time series from the preprocessed postseismic GNSS position time series yielded seasonally corrected east, north, and vertical time series for the subsequent extraction of postseismic decay deformation.

3.2 Extraction of three-dimensional postseismic decay signals

Following seasonal correction, we applied vbICA separately to the east, north, and vertical GNSS position time series from all 32 stations to extract postseismic decay deformation associated with the 2021 Mw 7.4 Maduo earthquake. The ARD curves and cumulative explained variance supported retaining two independent components for the east component and three independent components for both the north and vertical components (Figs. S9-S11). The temporal functions and spatial responses of the retained components are shown in Figs. 6-8.

In the east-component decomposition, IC1 showed a clear onset at the earthquake epoch, followed by rapid postseismic change and a progressively decreasing rate of change. Its spatial responses were concentrated around the epicentral area and the coseismic rupture zone (Fig. 6a). IC2 showed irregular temporal variations without a sustained postseismic decay pattern and did not show a corresponding spatial concentration (Fig. 6b). We therefore used the IC1 from the east-component decomposition to reconstruct the east postseismic decay deformation time series at all stations. In the north-component decomposition, IC1 exhibited a postseismic decay pattern and spatial responses concentrated near the rupture zone (Fig. 7a), whereas IC2 and IC3 lacked a stable postseismic decay pattern and showed more spatially variable responses (Figs. 7b and 7c). We used the IC1 from the north-component decomposition to reconstruct the north postseismic decay deformation time series.

Fig. 6. Separate vbICA decomposition of the seasonally corrected east-component GNSS position time series for postseismic deformation extraction. Panels (a) and (b) show IC1 and IC2, respectively. Each panel contains the spatial response U in the upper map and the corresponding temporal function V in the lower plot. Open circles and blue triangles denote continuous GNSS stations installed before and after the earthquake, respectively. The red star marks the epicentre of the 2021 Mw 7.4 Maduo earthquake. Red dashed lines denote the mapped coseismic surface rupture in the maps and the

earthquake epoch in the temporal-function plots. Arrows show east-component spatial responses, and the reference vector is given in each map. The abrupt variation in the IC2 temporal function around 2023 is likely associated with data gaps at several stations before that time. S is the component-specific scaling factor used to reconstruct station displacement time series and is expressed in millimetres.

Fig. 7. Separate vbICA decomposition of the seasonally corrected north-component GNSS position time series for postseismic deformation extraction. Panels (a)-(c) show IC1-IC3, respectively. The spatial responses and temporal functions are arranged as in Fig. 6; arrows show north-component spatial responses. All symbols and line styles are defined in Fig. 6.

The vertical-component decomposition retained three independent components (Fig. 8). The temporal function of IC1 showed a postseismic change after the earthquake and an overall decrease in its rate of change during the postseismic interval, but pronounced short-period fluctuations remained superimposed on this temporal evolution. Its temporal function was therefore less smooth than the IC1 temporal functions obtained from the east- and north-component decompositions. Similar short-period fluctuations occurred in the vertical time series at several stations and may therefore have contributed to the common temporal function recovered as IC1. These fluctuations may reflect residual nontectonic or observational variations that were not fully separated from the postseismic signal; their source cannot be determined from the present decomposition alone. The vertical spatial responses of IC1 were heterogeneous across the network: positive responses predominated at stations around the central rupture segment, whereas several stations outside this area showed weaker or negative responses. IC2 and IC3 were dominated by irregular short-period fluctuations, did not show a sustained postseismic temporal evolution, and had spatial responses with substantial station-to-station variability (Figs. 8b and 8c). We therefore selected IC1, which retained both the sustained postseismic temporal evolution and the spatial response associated with the rupture region, to reconstruct the vertical postseismic decay deformation time series.

Fig. 8. Separate vbICA decomposition of the seasonally corrected vertical-component GNSS position time series for postseismic deformation extraction. Panels (a)-(c) show IC1-IC3, respectively. The spatial responses and temporal functions are arranged as in Fig. 6; upward and downward arrows show positive and negative vertical spatial responses. All symbols and line styles are defined in Fig. 6.

Using the IC1 selected from each directional decomposition, we reconstructed the east, north, and vertical postseismic decay deformation time series at all stations. Representative reconstructions at QHMD and NEFT, which were installed before and after the earthquake, respectively, show that the horizontal IC1 reconstructions capture the principal postseismic changes after preprocessing and seasonal correction, whereas the vertical reconstruction retains the longer-term postseismic change despite stronger short-period variability (Fig. 9). We then fitted the reconstructed component-wise time series to estimate the two-year cumulative postseismic displacement fields shown in Fig. 10.

Fig. 9. Examples of time-series preprocessing, seasonal correction, and postseismic deformation reconstruction at stations QHMD and NEFT. The upper panels show the east, north, and vertical coordinate time series at QHMD, and the lower panels show the corresponding postseismic time series at NEFT. Light-grey curves show the original coordinate time series in the ITRF2014 reference frame; red curves show the estimated long-term linear trends; green curves show the reconstructed seasonal displacement time series; and dark-grey curves show the time series after removal of the long-term trend and reconstructed seasonal displacement. Blue curves show the corresponding offset-corrected time series. Black curves show the postseismic deformation reconstructed from IC1 in the respective east-, north-, and vertical-component vbICA decompositions. The vertical dashed line marks the 2021 Mw 7.4 Maduo earthquake.

Fig. 10. Two-year cumulative postseismic displacement field estimated from fits to the east, north, and vertical time series reconstructed from IC1 in the separate component-wise vbICA decompositions. Arrows show horizontal displacements, and colour-coded circles show vertical displacements. The horizontal-vector reference scale is 20 mm, with

a plotted uncertainty of +/-5 mm. The red star marks the epicentre of the 2021 Mw 7.4 Maduo earthquake, and grey lines denote major active faults.

4. Discussions

4.1 Stability of the extracted postseismic decay signal

The component-wise east, north, and vertical decompositions described in Section 3.2 provide the primary postseismic reconstructions in this study. To evaluate their stability, we also applied joint three-component vbICA. We first applied vbICA to the preprocessed three-component GNSS position time series spanning the pre-earthquake and postseismic intervals at the 19 continuous stations installed before the earthquake to identify regional seasonal components. We selected the seasonal components on the basis of their temporal functions, spectral characteristics, and spatial responses. For the 19 stations, we reconstructed the postseismic seasonal time series directly from the postseismic portions of the corresponding temporal functions, spatial responses, and weights. For the 13 stations installed after the earthquake, we interpolated the spatial responses of the selected seasonal components to the station locations using Kriging and combined them with the corresponding postseismic temporal functions and weights to reconstruct the seasonal time series. After subtracting the reconstructed seasonal time series from the preprocessed postseismic three-component GNSS time series at all 32 stations, we applied joint three-component vbICA to extract a joint postseismic decay component. The ARD analysis and reconstruction results indicated that a two-component solution adequately captured the major variations (Fig. S12). Within this joint solution, IC1 exhibited a postseismic decay pattern beginning at the earthquake epoch, and its spatial response was concentrated around the epicentral area and near the coseismic rupture zone (Figs. S13a and S13c). IC2 did not show comparable temporal or spatial characteristics (Figs. S13b and S13d). We therefore used the joint IC1 to reconstruct the three-component postseismic decay deformation time series and compared them with the component-wise reconstructions.

Comparison of the single-component decompositions, the joint three-component decomposition, and the trajectory-model estimates shows close agreement in postseismic time evolution for both the east and north components (Fig. 11). Station-wise statistics

summarized in Table S1 show that the correlations between the single-component and joint reconstructions are consistently high, with values of 0.9921 in the east component and 0.9828 in the north component. The corresponding root-mean-square differences range from 0.15 to 2.98 mm in the east component and from 0.22 to 1.65 mm in the north component, while the absolute differences in two-year cumulative displacement range from 0.12 to 2.87 mm and from 0.15 to 2.06 mm, respectively. Within each component, these identical correlation coefficients arise because the station-specific reconstructions within each vbICA solution are scalings of its common IC1 temporal function, determined by the station-specific spatial responses and weights. Accordingly, the correlations quantify the similarity between the IC1 temporal functions recovered by the two decomposition strategies, whereas the root-mean-square and cumulative-displacement differences quantify station-dependent differences in reconstructed amplitude. The single-component reconstructions also agree closely with the logarithmic postseismic terms from station-wise parameterized trajectory models fitted to the detrended GNSS time series published by Xiong (2025). Correlations range from 0.9347 to 0.9881 in the east component and from 0.9502 to 0.9887 in the north component, with root-mean-square differences of 0.29~3.23 mm and 0.31~2.58 mm and absolute differences in two-year cumulative displacement of 0.14~3.39 mm and 0.09~2.48 mm, respectively. The larger differences at some stations relative to the fitted curves may reflect differences in GNSS time-series processing and in the representation of postseismic deformation by data-driven decomposition and parameterized trajectory models. Thus, the agreement among the three estimates indicates that the single-component decompositions robustly extract the horizontal postseismic decay signal, which is not controlled by the decomposition strategy or by anomalies at individual stations.

Fig. 11. Comparison of horizontal postseismic decay time series obtained from the separate component-wise vbICA decompositions, the joint three-component vbICA decomposition, and station-wise trajectory models. Grey symbols show detrended GNSS observations. Cyan dashed curves show the component-wise vbICA reconstructions, red curves show the joint three-component vbICA reconstructions, and dark-blue dash-dotted curves show the logarithmic postseismic terms from station-wise trajectory models fitted to the detrended GNSS time series made available by Xiong (2025). East (E) and north (N) components are shown for six representative stations. Time is given in days after the 2021 Mw 7.4 Maduo earthquake, and displacement is in millimetres.

For the vertical component, InSAR-derived vertical time series at GNSS station locations provide independent pointwise comparisons of vertical displacement evolution. By comparison, the displacement directions of both vbICA reconstructions are broadly consistent with the InSAR results, whereas the single-component U reconstruction generally yields cumulative vertical displacements smaller than those from the joint three-component decomposition and closer in amplitude to the InSAR time series (Fig. 12; Liu, 2023). The observed amplitude difference may arise because the joint decomposition estimates common components from the three coordinate time series simultaneously; differences in signal amplitude, noise level, and residual variability among components may affect the reconstructed vertical component, potentially causing an overestimation of vertical postseismic change in the joint decomposition. These results also indicate that the vertical reconstruction is more sensitive to the decomposition strategy than the horizontal reconstruction and support the use of the single-component decomposition to extract vertical postseismic decay deformation.

Fig. 12. Comparison of vertical postseismic displacement time series obtained from the component-wise vertical vbICA decomposition, the joint three-component vbICA decomposition, and InSAR observations at GNSS station locations. Grey symbols show detrended GNSS observations. Cyan dashed curves show the component-wise vertical vbICA reconstructions, red curves show the joint three-component vbICA reconstructions, and dark-blue dash-dotted curves show the InSAR-derived vertical time series from Liu (2023). Time is given in days after the 2021 Mw 7.4 Maduo earthquake, and displacement is in millimetres.

4.2 Applicability and limitations of vbICA for postseismic GNSS time-series analysi

vbICA provides a useful approach for postseismic GNSS time-series processing because it identifies components with common temporal variations and spatial responses from multi-station observations without prescribing a postseismic decay function or a fixed seasonal model (Choudrey, 2002; Gualandi et al., 2016, 2017). This property is relevant to continuous GNSS records from the Tibetan Plateau, in which deformation and non-tectonic signals may overlap. Compared with conventional single-station trajectory models that fit linear trends and prescribed annual and semiannual terms (Blewitt and Lavallée, 2002; Bevis and Brown, 2014), vbICA exploits common variations among multi-station GNSS observations. When time series with short observation spans or no

observations before the earthquake are analysed jointly with continuous GNSS stations whose records span the earthquake, these common variations can assist the separation of components that are otherwise insufficiently constrained by an individual record.

In the Maduo data set, regional seasonal components and postseismic decay deformation exhibited distinct temporal functions and spatial responses, indicating that vbICA can distinguish regional periodic variations from earthquake-related decay deformation in multi-station GNSS time series. Accordingly, vbICA can also identify regional seasonal displacement components in continuous GNSS records during interseismic periods. Such components can be compared with hydrological and other surface-loading models to examine their temporal evolution and spatial variability (Serpelloni et al., 2018; White et al., 2022). Observations of freeze-thaw processes and local surface conditions can provide complementary information for their interpretation (Daout et al., 2017). However, a separated seasonal component cannot be directly attributed to a specific environmental process based solely on the decomposition result; its geophysical origin requires assessment through comparison with independent observations and models.

The data-driven nature of vbICA also constrains the physical interpretation of the separated components. The method represents the observations as linear mixtures of statistically independent components; departures from these assumptions can reduce the separability of signals with similar temporal behaviour. ARD and reconstruction statistics guide the selection of the retained number of components. They do not automatically assign geophysical meaning to individual ICs. Component interpretation therefore requires joint examination of temporal functions, spectral characteristics, spatial responses, and reconstructed station time series; the extracted ICs represent statistical decompositions rather than physically attributed deformation processes. Component recovery can be affected when temporal and spatial signatures are insufficiently distinct, or when signal-to-noise and source-to-source amplitude ratios are unfavourable and the network contains missing observations (Choudrey, 2002; Gualandi et al., 2016). The vertical comparison for the Maduo data set illustrates this limitation in the joint three-component decomposition (Fig. 12): the horizontal components remain consistent between the joint and single-component decompositions, whereas the vertical component is more sensitive to the decomposition strategy. In the Maduo data set, the joint decomposition estimates common components from the three coordinate time series simultaneously, and differences in signal amplitude, noise level, and residual variability among components may affect the reconstructed vertical component. Accordingly,

vbICA results should be evaluated together with reconstructed time series, alternative decompositions, and independent deformation observations. Statistical separation alone cannot replace physical models and independent data when interpreting postseismic deformation mechanisms or environmental loading processes.

4.3 Implications for GNSS-based postseismic deformation analysis on the Tibetan Plateau

Postseismic deformation studies on the Tibetan Plateau increasingly benefit from the complementary use of spatially dense InSAR deformation fields and three-dimensional GNSS displacement time series (Bürgmann et al., 2000; Bock and Melgar, 2016; Bekaert et al., 2016). InSAR resolves the spatial distribution of deformation over broad areas, whereas GNSS records the temporal evolution of three-dimensional displacement at individual stations in a terrestrial reference frame (Herring et al., 2016; Fuhrmann and Garthwaite, 2019). The Maduo results show that common-component separation can characterize the temporal evolution of postseismic decay deformation in multi-station GNSS records and reveal differences in the stability of the horizontal and vertical components. The separated postseismic components can be compared with model predictions for postseismic deformation involving afterslip and viscoelastic relaxation, whereas the seasonal components can be evaluated against hydrological and other surface-loading models and observations of freeze-thaw processes and local surface conditions (Gualandi et al., 2017; Liu-Zeng et al., 2020; Serpelloni et al., 2018; White et al., 2022). GNSS can also link station-scale three-dimensional displacement with InSAR-derived deformation fields, help tie InSAR to a terrestrial reference frame, characterize long-wavelength residuals, and assess vertical displacement estimates (Bekaert et al., 2016; Fuhrmann and Garthwaite, 2019). Independent-component analysis has also been applied to postseismic GNSS time series in Nepal and to regional seasonal deformation in China (Gualandi et al., 2017; Yan et al., 2019). The Maduo case illustrates the relevance of common-component separation where postseismic decay and regional seasonal variations coexist in multi-station GNSS records from the Tibetan Plateau.

5. Conclusions

The postseismic deployment of 13 continuous GNSS stations after the 2021 Mw 7.4 Maduo earthquake, together with records from 19 continuous GNSS stations installed before the earthquake, provided an opportunity to assess vbICA for extracting postseismic decay deformation at stations without pre-earthquake records. Regional seasonal components were identified separately from the preprocessed east, north, and vertical time series during the pre-earthquake interval at the 19 continuous GNSS stations. We reconstructed the corresponding seasonal displacement time series at all stations and removed them from the postseismic time series before separate vbICA decompositions of the east, north, and vertical components. The component-wise horizontal reconstructions showed an exponential-shaped postseismic transient, with the rate of change decaying rapidly during the first year and approaching a near-steady level over the remainder of the observation period; the associated spatial responses were concentrated around the epicentral area and coseismic rupture zone. Horizontal reconstructions were consistent across the single-component and joint three-component decompositions and with trajectory-model estimates. In contrast, the vertical component did not show an equally clear exponential-shaped transient and was more sensitive to the decomposition strategy; the amplitude of the single-component U reconstruction was closer to the InSAR-derived vertical time series, whereas the joint three-component decomposition may overestimate the vertical amplitude. For continuous GNSS studies on the Tibetan Plateau, vbICA can exploit common variations in multi-station time series not only to extract postseismic decay deformation but also to separate regional seasonal displacement components for interseismic analyses.

Declarations

Ethics approval and consent to participate:

Not applicable

Consent for publication

No applicable

Availability of data and materials

The GNSS time series analysed in this study are publicly available through the Zenodo repository at https://doi.org/10.5281/zenodo.21969838.

Competing interests

The authors declare that they have no competing interests.

Funding

This work was supported by the International (Regional) Cooperation and Exchange Program of the National Natural Science Foundation of China (Grant No. W2411033).

Authors' contributions

Zhijun Liu conducted the GNSS data processing and analysis and wrote the original draft. Jing Liu-Zeng and Qiang Qiu contributed to the analysis and interpretation of the results and reviewed the manuscript. Yunfeng Tian and Bin Zhao reviewed the manuscript. Zhijun Liu, Peng Wang, Wenqian Yao, Yanxiu Shao, Wenxin Wang, and Longfei Han contributed to GNSS data collection. All authors read and approved the final manuscript.

Acknowledgements

This work was supported by the International (Regional) Cooperation and Exchange Program of the National Natural Science Foundation of China (Grant No. W2411033). We sincerely thank Prof. Kejie Chen of Southern University of Science and Technology for providing GNSS data from selected stations and Dr. Zhiwei Fang of China University

of Geosciences (Wuhan) for valuable suggestions.

Authors' information

[1]Institute of Surface-Earth System Science, School of Earth System Science, Tianjin University, Tianjin, 300072, China

References

Altamimi Z, Rebischung P, Métivier L, Collilieux X (2016) ITRF2014: A new release of the International Terrestrial Reference Frame modeling nonlinear station motions. J Geophys Res Solid Earth 121:6109–6131. doi:10.1002/2016JB013098

Avouac J-P, Tapponnier P (1993) Kinematic model of active deformation in Central Asia. Geophys Res Lett 20:895–898. doi:10.1029/93GL00128

Bekaert DPS, Segall P, Wright TJ, Hooper AJ (2016) A network inversion filter combining GNSS and InSAR for tectonic slip modeling. J Geophys Res Solid Earth 121:2069–2086. doi:10.1002/2015JB012638

Bevis M, Brown A (2014) Trajectory models and reference frames for crustal motion geodesy. J Geod 88:283–311. doi:10.1007/s00190-013-0685-5

Blewitt G, Lavallée D (2002) Effect of annual signals on geodetic velocity. J Geophys Res Solid Earth 107(B7):2145. doi:10.1029/2001JB000570

Bock Y, Melgar D (2016) Physical applications of GPS geodesy: A review. Rep Prog Phys 79:106801. doi:10.1088/0034-4885/79/10/106801

Böhm J, Niell A, Tregoning P, Schuh H (2006) The Global Mapping Function (GMF): A new empirical mapping function based on numerical weather model data. Geophys Res Lett 33:L07304. doi:10.1029/2005GL025546

Böhm J, Werl B, Schuh H (2006) Troposphere mapping functions for GPS and very long baseline interferometry from European Centre for Medium-Range Weather Forecasts operational analysis data. J Geophys Res Solid Earth 111:B02406. https://doi.org/10.1029/2005JB003629

Bos MS, Fernandes RMS, Williams SDP, Bastos L (2013) Fast geodetic time series analysis with missing data. J Geod 87:351–360. doi:10.1007/s00190-012-0605-0

Bürgmann R, Rosen PA, Fielding EJ (2000) Synthetic aperture radar interferometry to measure Earth's surface topography and its deformation. Annu Rev Earth Planet Sci 28:169–209. doi:10.1146/annurev.earth.28.1.169

Bürgmann R, Thatcher W (2013) Space geodesy: A revolution in crustal deformation measurements of tectonic processes. Geol Soc Am Spec Pap 500:397–430. doi:10.1130/2013.2500(12)

Choudrey RA (2002) Variational methods for Bayesian independent component analysis. PhD thesis, University of Oxford, Oxford

Cressie N (1993) Statistics for spatial data, revised edn. Wiley, New York

Daout S, Doin M-P, Peltzer G, Socquet A, Lasserre C (2017) Large-scale InSAR monitoring of permafrost freeze-thaw cycles on the Tibetan Plateau. Geophys Res Lett 44:901–909. doi:10.1002/2016GL070781

Diao F, Wang R, Xiong X, Liu C (2021) Overlapped postseismic deformation caused by afterslip and viscoelastic relaxation following the 2015 Mw 7.8 Gorkha (Nepal) earthquake. J Geophys Res Solid Earth 126:e2020JB020378. doi:10.1029/2020JB020378

Dong D, Fang P, Bock Y, Cheng MK, Miyazaki S (2002) Anatomy of apparent seasonal variations from GPS-derived site position time series. J Geophys Res Solid Earth 107:B4, 2075. doi:10.1029/2001JB000573

Fu Y, Freymueller JT (2012) Seasonal and long-term vertical deformation in the Nepal Himalaya constrained by GPS and GRACE measurements. J Geophys Res Solid Earth 117:B03407. doi:10.1029/2011JB008925

Fuhrmann T, Garthwaite MC (2019) Resolving three-dimensional surface motion with InSAR: Constraints from multi-geometry data fusion. Remote Sens 11:241. doi:10.3390/rs11030241

Gan W, Zhang P, Shen Z-K, Niu Z, Wang M, Wan Y, Zhou D, Cheng J (2007) Present-day crustal motion within the Tibetan Plateau inferred from GPS measurements. J Geophys Res Solid Earth 112:B08416. doi:10.1029/2005JB004120

Gualandi A, Avouac J-P, Galetzka J, Genrich JF, Blewitt G, Adhikari LB, Koirala BP, Gupta R, Upreti BN, Pratt-Sitaula B, Liu-Zeng J (2017) Pre- and post-seismic deformation related to the 2015, Mw 7.8 Gorkha earthquake, Nepal. Tectonophysics 714–715:90–106. doi:10.1016/j.tecto.2016.06.014

Gualandi A, Serpelloni E, Belardinelli ME (2016) Blind source separation problem in GPS time series. J Geod 90:323–341. doi:10.1007/s00190-015-0875-4

Herring TA, King RW, Floyd MA, McClusky SC (2018) GAMIT/GLOBK reference manual, release 10.7. Massachusetts Institute of Technology, Cambridge, MA

Herring TA, Melbourne TI, Murray MH, Floyd MA, Szeliga WM, King RW, Phillips DA, Puskas CM, et al (2016) Plate Boundary Observatory and related networks: GPS data analysis methods and geodetic products. Rev Geophys 54:759–808. doi:10.1002/2016RG000529

Jin Z, Fialko Y (2021) Coseismic and early postseismic deformation due to the 2021 M7.4 Maduo (China) earthquake. Geophys Res Lett 48:e2021GL095213. doi:10.1029/2021GL095213

Jin Z, Fialko Y, Yang H, Li Y (2023) Transient deformation excited by the 2021 M7.4 Maduo (China) earthquake: Evidence of a deep shear zone. J Geophys Res Solid Earth 128:e2023JB026643. doi:10.1029/2023JB026643

Kłos A, Bos MS, Bogusz J (2018) Detecting time-varying seasonal signal in GPS position time series with different noise levels. GPS Solut 22:21. doi:10.1007/s10291-017-0686-6

Larochelle S, Gualandi A, Chanard K, Avouac J-P (2018) Identification and extraction of seasonal geodetic signals due to surface load variations. J Geophys Res Solid Earth 123:11031–11047. doi:10.1029/2018JB016607

Li Z, Xiong W, Hooper A, Zhao Z, Gao Y, Elliott JR, Wright T, Yue H, Wang T (2025) Imaging viscosity after the 2021 Mw 7.4 Maduo earthquake: Insights on the regional rheology variation beneath the Bayan Har block. Earth Planet Sci Lett 666:119465. doi:10.1016/j.epsl.2025.119465

Liu J (2023) The two-year InSAR postseismic displacements of the 2021 Maduo earthquake [data set]. Zenodo. doi:10.5281/zenodo.10404888

Liu-Zeng J, Liu Z, Liu X, Milliner C, Rodríguez Padilla AM, Xu S, Avouac J-P, Yao W, et al (2024) Fault orientation trumps fault maturity in controlling coseismic rupture characteristics of the 2021 Maduo earthquake. AGU Adv 5:e2023AV001134. doi:10.1029/2023AV001134

Liu-Zeng J, Yao W, Liu X, Shao Y, Wang W, Han L, Wang Y, Zeng X, Li J, Wang Z (2022) High-resolution structure-from-motion models covering 160 km-long surface ruptures of the 2021 Mw 7.4 Madoi earthquake in northern Qinghai-Tibetan Plateau. Earthq Res Adv 2:100140. doi:10.1016/j.eqrea.2022.100140

Liu-Zeng J, Zhang Z, Rollins C, Gualandi A, Avouac J-P, Shi H, et al (2020) Postseismic deformation following the 2015 Mw 7.8 Gorkha (Nepal) earthquake: New GPS data, kinematic and dynamic models, and the roles of afterslip and viscoelastic relaxation. J Geophys Res Solid Earth 125:e2020JB019852. doi:10.1029/2020JB019852

Lyard F, Lefèvre F, Letellier T, Francis O (2006) Modelling the global ocean tides: Modern insights from FES2004. Ocean Dyn 56:394–415. doi:10.1007/s10236-006-0086-x

Molnar P, Tapponnier P (1975) Cenozoic tectonics of Asia: Effects of a continental collision. Science 189:419–426. doi:10.1126/science.189.4201.419

Nield GA, King MA, Koulali A, Samrat N (2023) Postseismic deformation in the Northern Antarctic Peninsula following the 2003 and 2013 Scotia Sea earthquakes. J Geophys Res Solid Earth 128:e2023JB026685. https://doi.org/10.1029/2023JB026685

Petit G, Luzum B (eds) (2010) IERS conventions (2010). IERS Technical Note 36. Verlag des Bundesamts für Kartographie und Geodäsie, Frankfurt am Main

Rebischung P, Altamimi Z, Ray J, Garayt B, Collilieux X (2016) The IGS contribution to ITRF2014. J Geod 90:611–630. doi:10.1007/s00190-016-0897-6

Ryder I, Bürgmann R, Pollitz F (2011) Lower crustal relaxation beneath the Tibetan Plateau and Qaidam Basin following the 2001 Kokoxili earthquake. Geophys J Int 187:613–630. doi:10.1111/j.1365-246X.2011.05179.x

Santamaría-Gómez A, Bouin M-N, Collilieux X, Wöppelmann G (2011) Correlated errors in GPS

794 position time series: Implications for velocity estimates. J Geophys Res Solid Earth 116:B01405.
795 doi:10.1029/2010JB007701
796 Serpelloni E, Pintori F, Gualandi A, Scoccimarro E, Cavaliere A, Anderlini L, Belardinelli ME,
797 Todesco M (2018) Hydrologically induced karst deformation: Insights from GPS measurements
798 in the Adria-Eurasia plate boundary zone. J Geophys Res Solid Earth 123:4413–4430.
799 doi:10.1002/2017JB015252
800 Stamps DS, Kreemer C (2024) Open access GNSS data for studies of the lithosphere. Geochem
801 Geophys Geosyst 25:e2024GC011567. doi:10.1029/2024GC011567
802 Tapponnier P, Xu Z, Roger F, Meyer B, Arnaud N, Wittlinger G, Yang J (2001) Oblique stepwise rise
803 and growth of the Tibet Plateau. Science 294:1671–1677. doi:10.1126/science.105978
804 Taylor M, Yin A (2009) Active structures of the Himalayan-Tibetan orogen and their relationships to
805 earthquake distribution, contemporary strain field, and Cenozoic volcanism. Geosphere 5:199–
806 214. doi:10.1130/GES00217.1
807 Tian Z, Freymueller J, Yang H, Ji G, Wang S, Li Z (2024) Postseismic deformation due to the 2021 M
808 7.4 Maduo (China) earthquake and implications for regional rheology and seismic hazards around
809 the Bayan Har block. Earth Planet Sci Lett 647:119059. doi:10.1016/j.epsl.2024.119059
810 Wang M, Shen Z-K (2020) Present-day crustal deformation of continental China derived from GPS
811 and its tectonic implications. J Geophys Res Solid Earth 125:e2019JB018774.
812 doi:10.1029/2019JB018774
813 Wang M, Shen Z-K, Wang Y-Z, Bürgmann R, Wang F, Zhang P-Z, et al (2021) Postseismic
814 deformation of the 2008 Wenchuan earthquake illuminates lithospheric rheological structure and
815 dynamics of eastern Tibet. J Geophys Res Solid Earth 126:e2021JB022399.
816 doi:10.1029/2021JB022399
817 White A, Gardner WP, Borsa AA, Argus DF, Martens HR (2022) A review of GNSS/GPS in
818 hydrogeodesy: Hydrologic loading applications and their implications for water resource research.
819 Water Resour Res 58:e2022WR032078. doi:10.1029/2022WR032078
820 Williams SDP, Bock Y, Fang P, Jamason P, Nikolaidis RM, Prawirodirdjo L, Miller M, Johnson DJ
821 (2004) Error analysis of continuous GPS position time series. J Geophys Res Solid Earth
822 109:B03412. doi:10.1029/2003JB002741
823 Xiang Y, Wang H, Chen Y, Xing Y (2021) GNSS imaging of strain rate changes and vertical crustal
824 motions over the Tibetan Plateau. Remote Sens 13:4937. doi:10.3390/rs13234937
825 Xiong W (2025) 2-year cGPS time series following the 2021 Maduo earthquake [data set]. Zenodo.
826 doi:10.5281/zenodo.15165598
827 Xiong W, Chen W, Wang D, Wen Y, Nie Z, Liu G, Wang D, Yu P, et al (2022) Coseismic slip and early
828 afterslip of the 2021 Mw 7.4 Maduo, China earthquake constrained by GPS and InSAR data.
829 Tectonophysics 840:229558. doi:10.1016/j.tecto.2022.229558

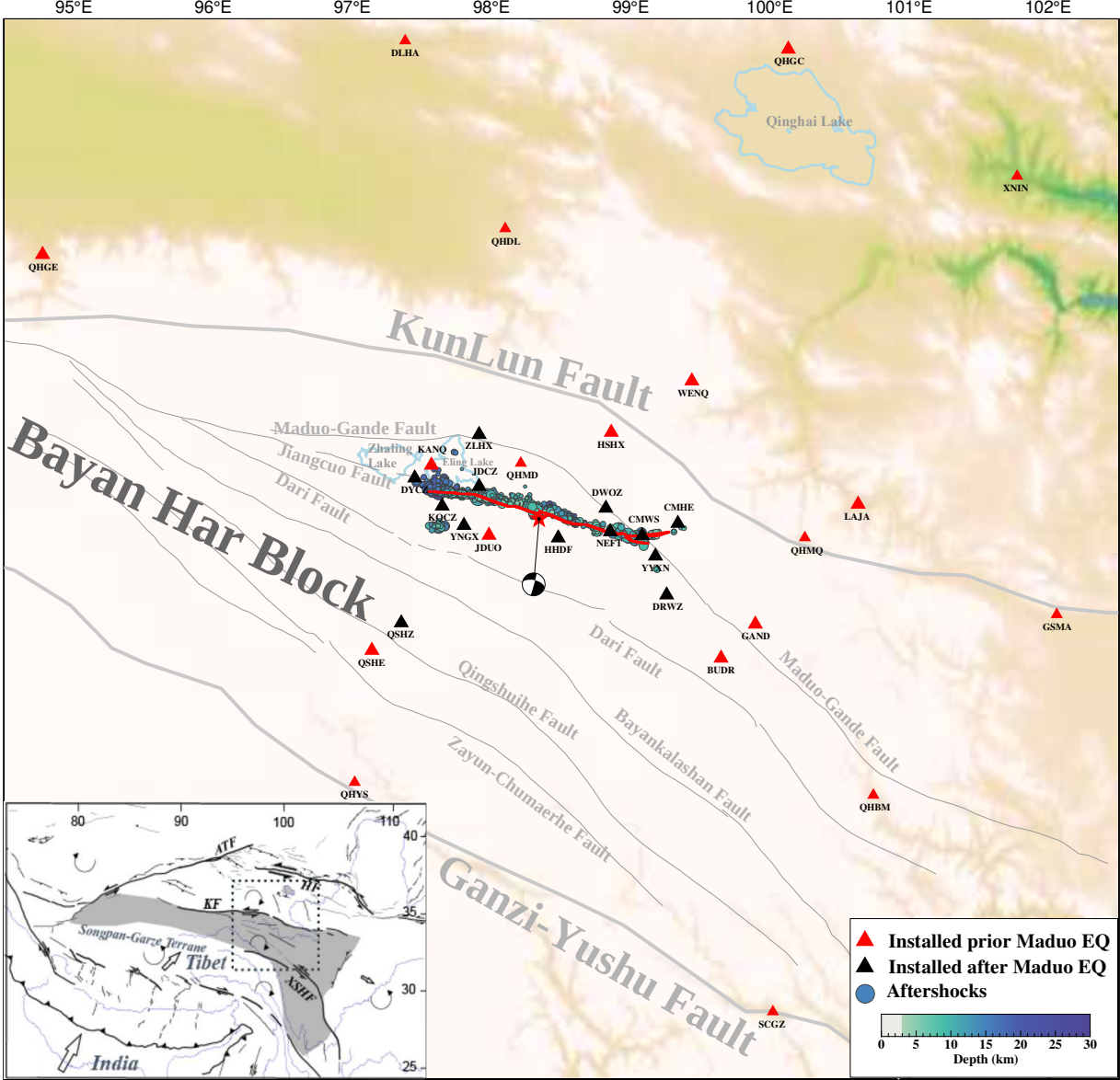
Xu L, Zhang Y, Chen J, Meng L, Fielding EJ, Zinke R, Bao H (2023) Understanding the rupture kinematics and slip model of the 2021 Mw 7.4 Maduo earthquake: A bilateral event on bifurcating faults. J Geophys Res Solid Earth 128:e2022JB025936. doi:10.1029/2022JB025936

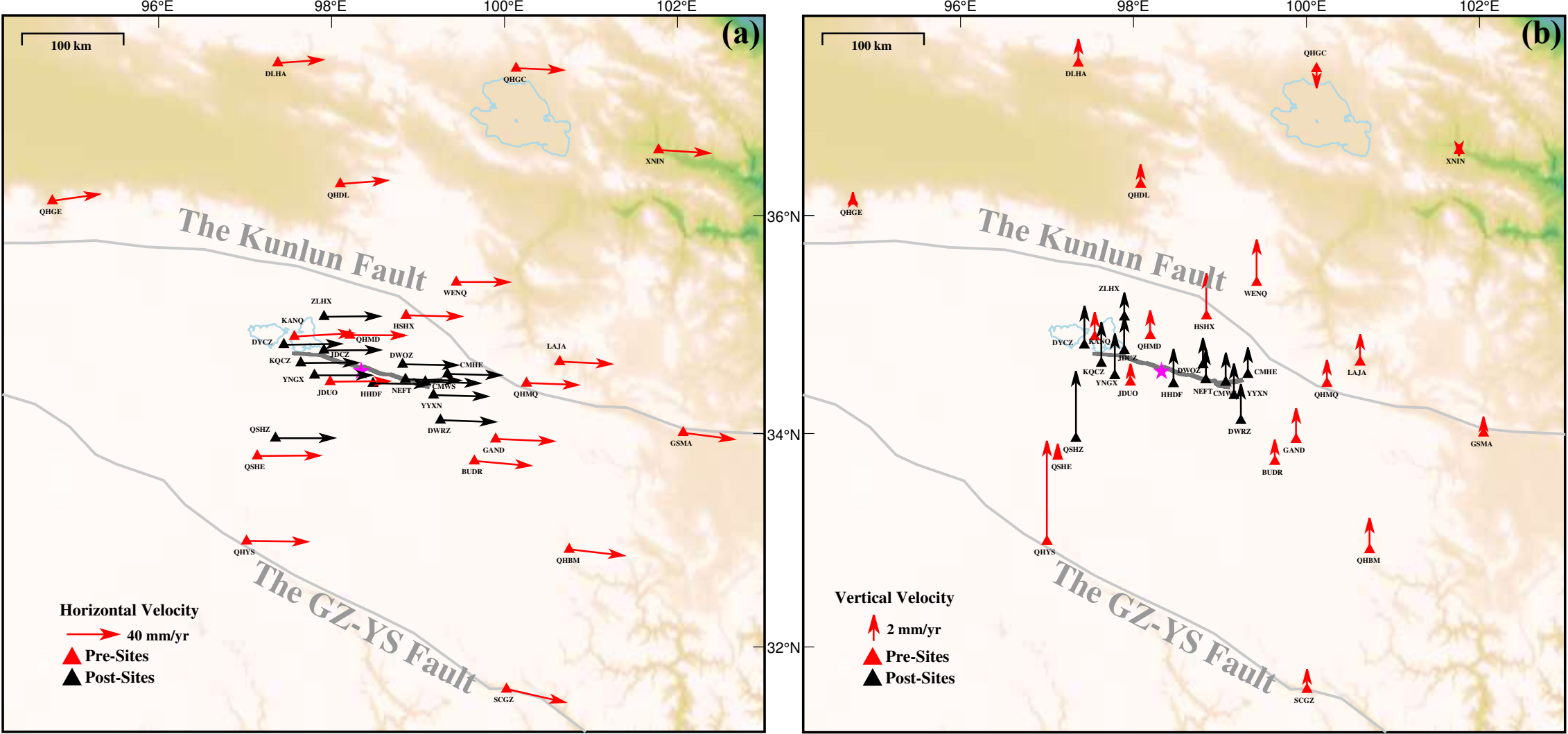
Yan J, Dong D, Bürgmann R, Materna K, Tan W, Peng Y, Chen J (2019) Separation of sources of seasonal uplift in China using independent component analysis of GNSS time series. J Geophys Res Solid Earth 124:11951–11971. doi:10.1029/2019JB018139

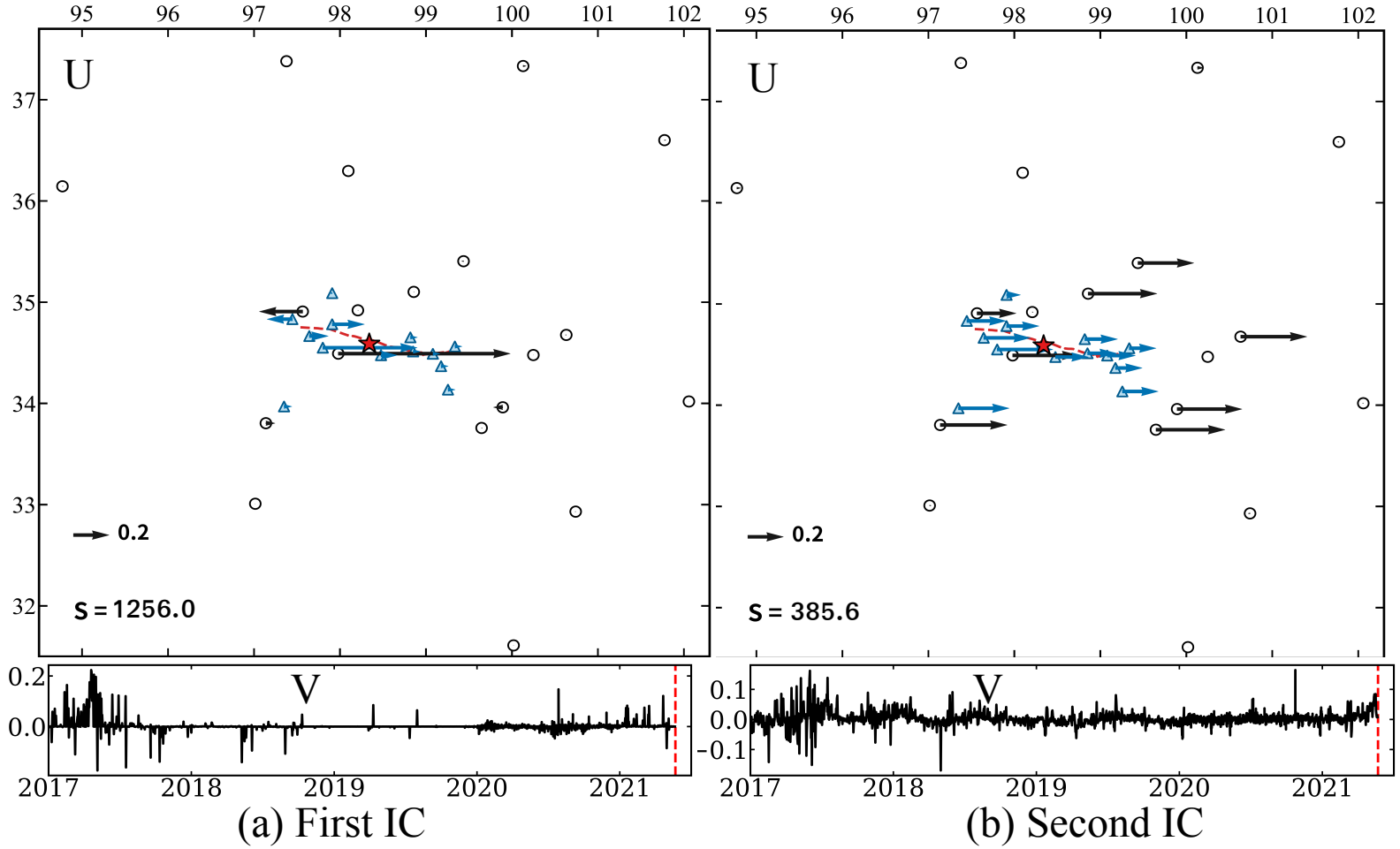
Yao W, Liu-Zeng J, Shi X, Wang Z, Rodríguez Padilla A, Qin K, Han L, Shao Y, Liu X, Xu J, Wang Y, Gao Y (2024) Rupture branching, propagation, and termination at the eastern end of the 2021 Mw 7.4 Maduo earthquake, northern Tibetan Plateau. Tectonophysics 876:230262. doi:10.1016/j.tecto.2024.230262

Yin A, Harrison TM (2000) Geologic evolution of the Himalayan-Tibetan orogen. Annu Rev Earth Planet Sci 28:211–280. doi:10.1146/annurev.earth.28.1.211

Zhang P-Z, Shen Z-K, Wang M, Gan W, Bürgmann R, Molnar P, Wang Q, Niu Z, Sun J, Wu J, Hanrong S (2004) Continuous deformation of the Tibetan Plateau from global positioning system data. Geology 32:809–812. doi:10.1130/G20554.1

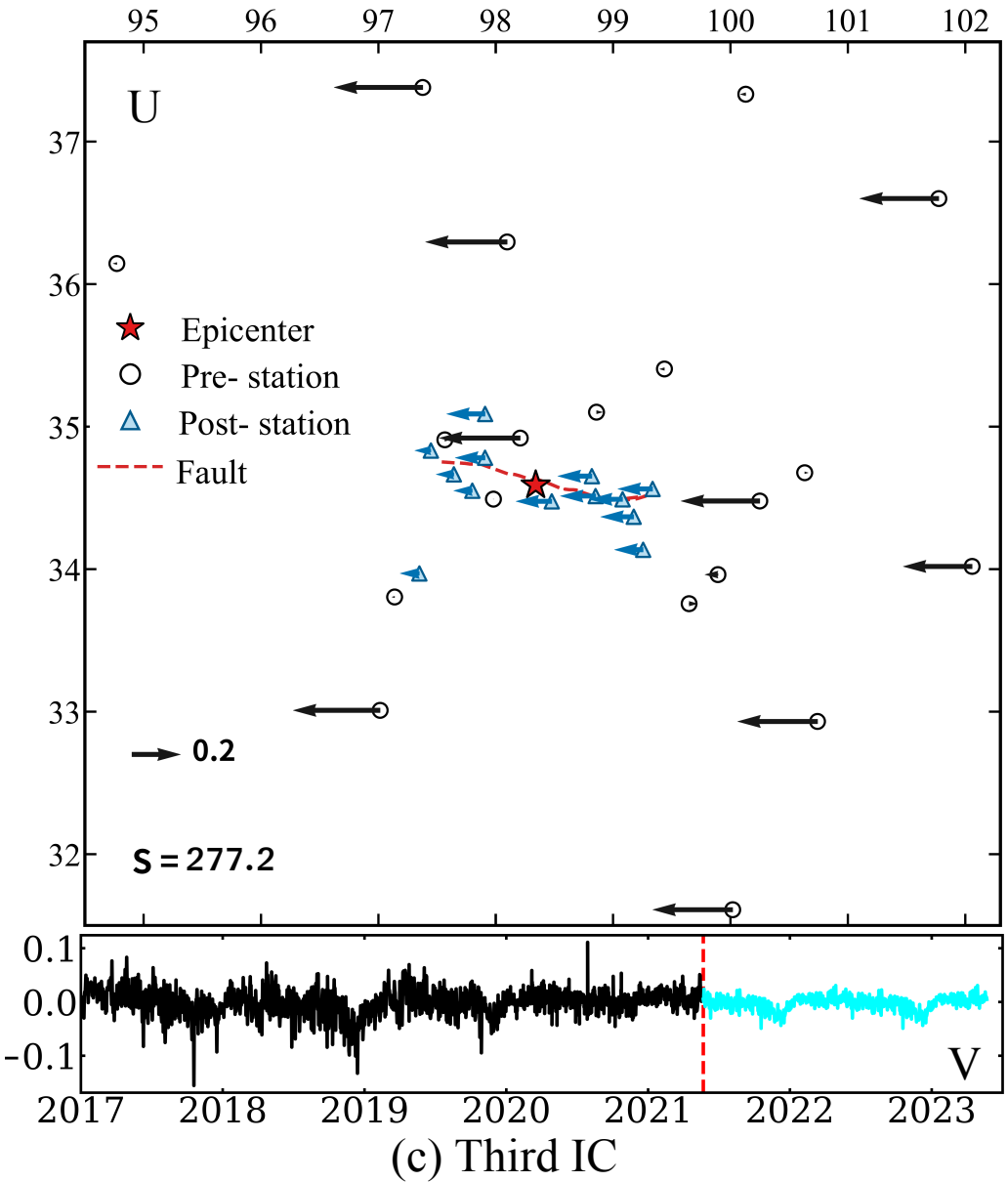

95°E
96°E
97°E
98°E
99°E
100°E
101°E
102°E
37°N
36°N
35°N
34°N
33°N
32°N
DLHA
QHGC
Qinghai Lake
XNIN
QHDL
QHGE
KunLun Fault
WENQ
Maduo-Gande Fault
Zhaling Lake
Eling Lake
Jiangcuo Fault
Dari Fault
Bayan Har Block
KANQ
ZLHX
HSHX
JDCZ
QHMD
DYCZ
DWOZ
CMHE
KQCZ
CMWS
YNGX
JDUO
HHDF
NEFT
YNSN
LAJA
QHMQ
DRWZ
GSMA
QSHZ
GAND
QSHE
BUDR
Dari Fault
Maduo-Gande Fault
Qingshuihe Fault
Bayankalashan Fault
Zayun-Chumaerhe Fault
QHYS
QHBM
Ganzi-Yushu Fault
SCGZ
Installed prior Maduo EQ
Installed after Maduo EQ
Aftershocks
0
5
10
15
20
25
30
Depth (km)
80
90
100
110
40
35
30
25
ATF
KF
HF
XSHF
Songpan-Garze Terrane
Tibet
India


(a)
100 km
96°E
98°E
100°E
102°E
36°N
34°N
32°N
DLHA
QHGC
XNIN
QHDL
QHGE
The Kunlun Fault
WENQ
ZLHX
KANQ
HSHX
DYCZ
QHMD
JDCZ
KQCZ
DWOZ
CMHE
YNGX
JDUO
HHDF
NEFT
CMWS
YYXN
LAJA
QHMQ
DWRZ
QSHZ
GAND
GSMA
QSHE
BUDR
QHYS
QHBM
The GZ-YS Fault
SCGZ
Horizontal Velocity
40 mm/yr
Pre-Sites
Post-Sites
(b)
100 km
96°E
98°E
100°E
102°E
DLHA
QHGC
XNIN
QHDL
QHGE
The Kunlun Fault
WENQ
ZLHX
HSHX
DYCZ
KANQ
QHMD
JDCZ
KQCZ
DWOZ
CMHE
YNGX
JDUO
HHDF
NEFT
CMWS
YYXN
LAJA
QHMQ
DWRZ
QSHZ
GAND
GSMA
QSHE
BUDR
QHYS
QHBM
The GZ-YS Fault
SCGZ
Vertical Velocity
2 mm/yr
Pre-Sites
Post-Sites

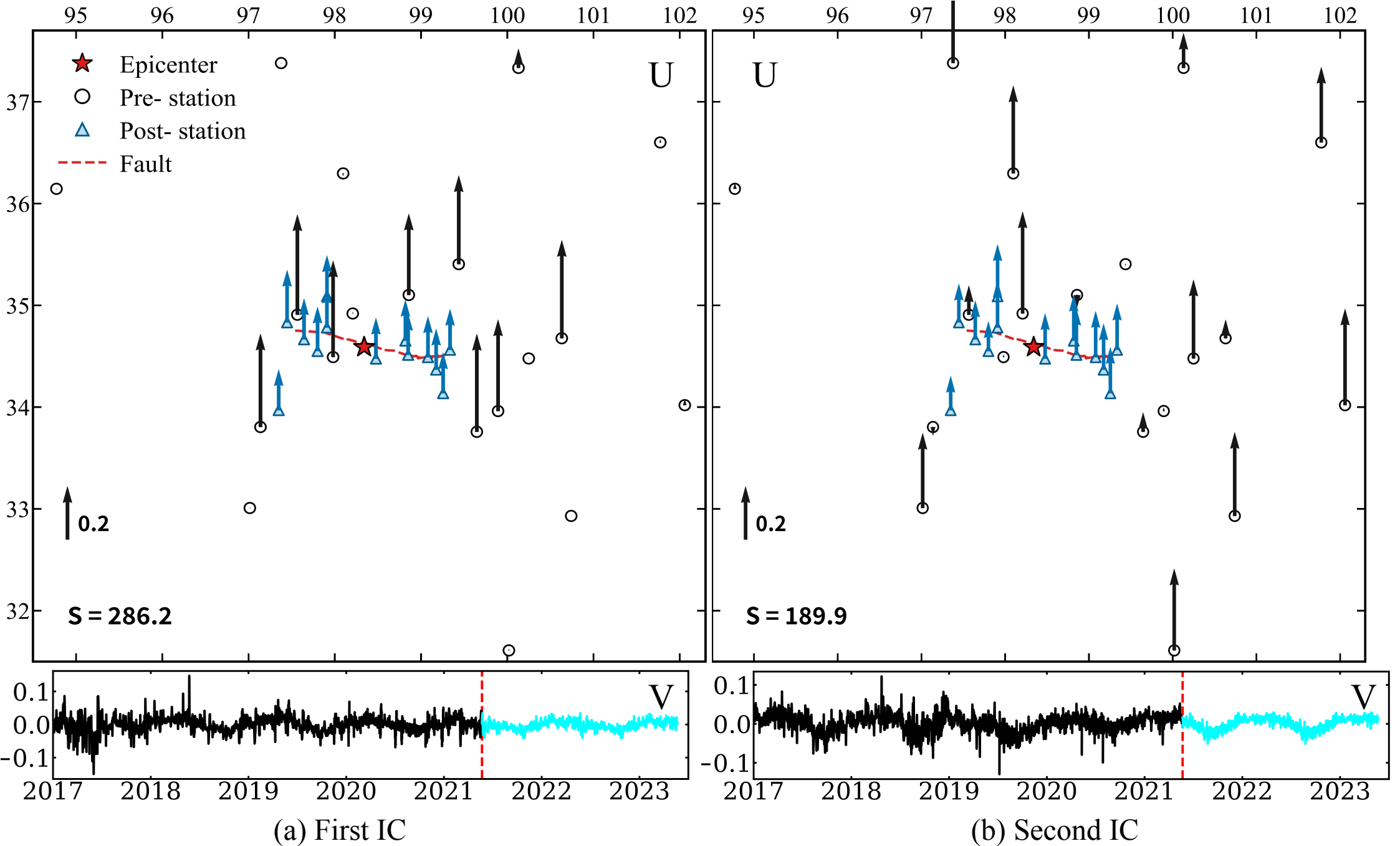


(a) First IC

(b) Second IC

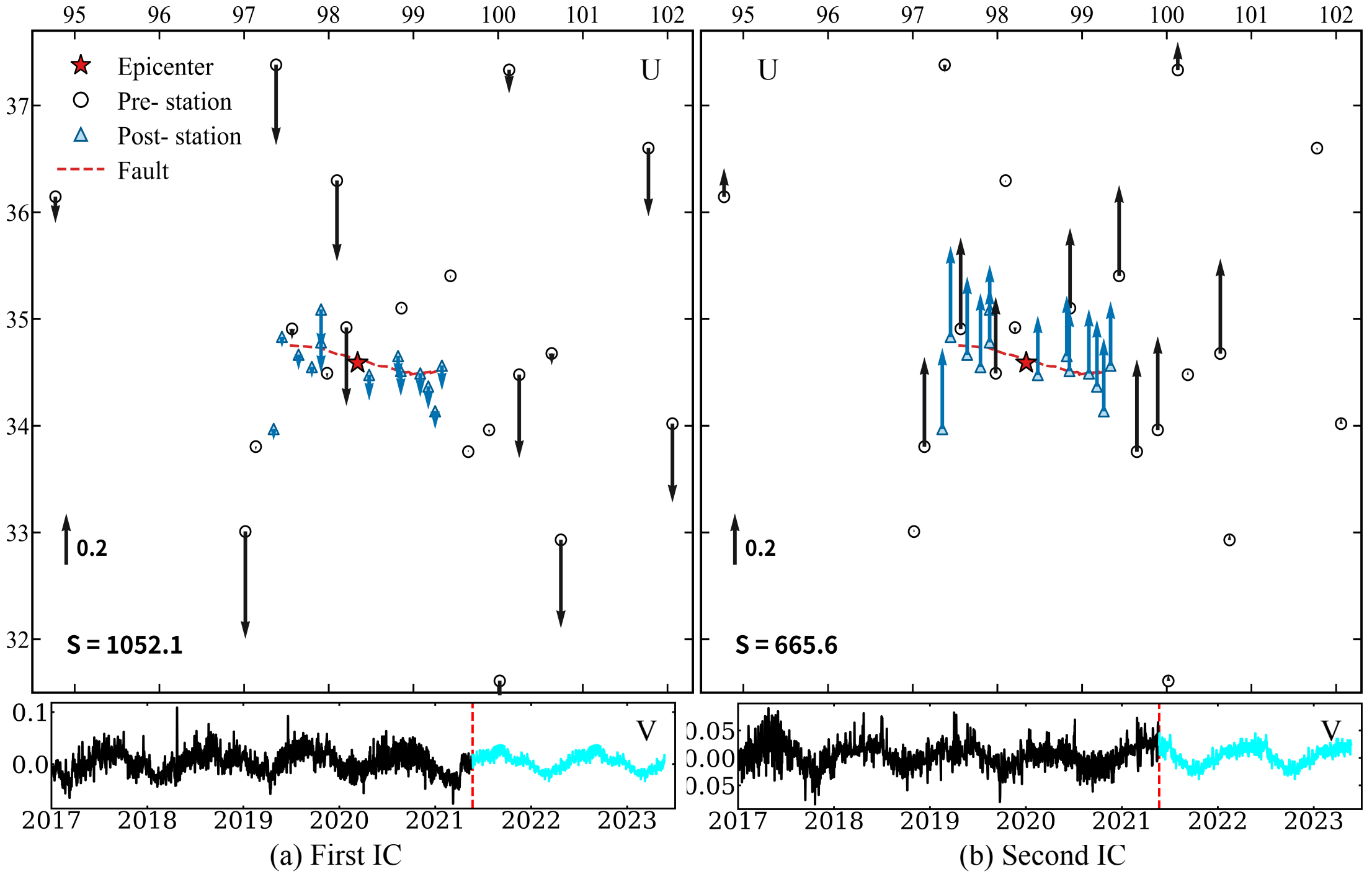


(c) Third IC



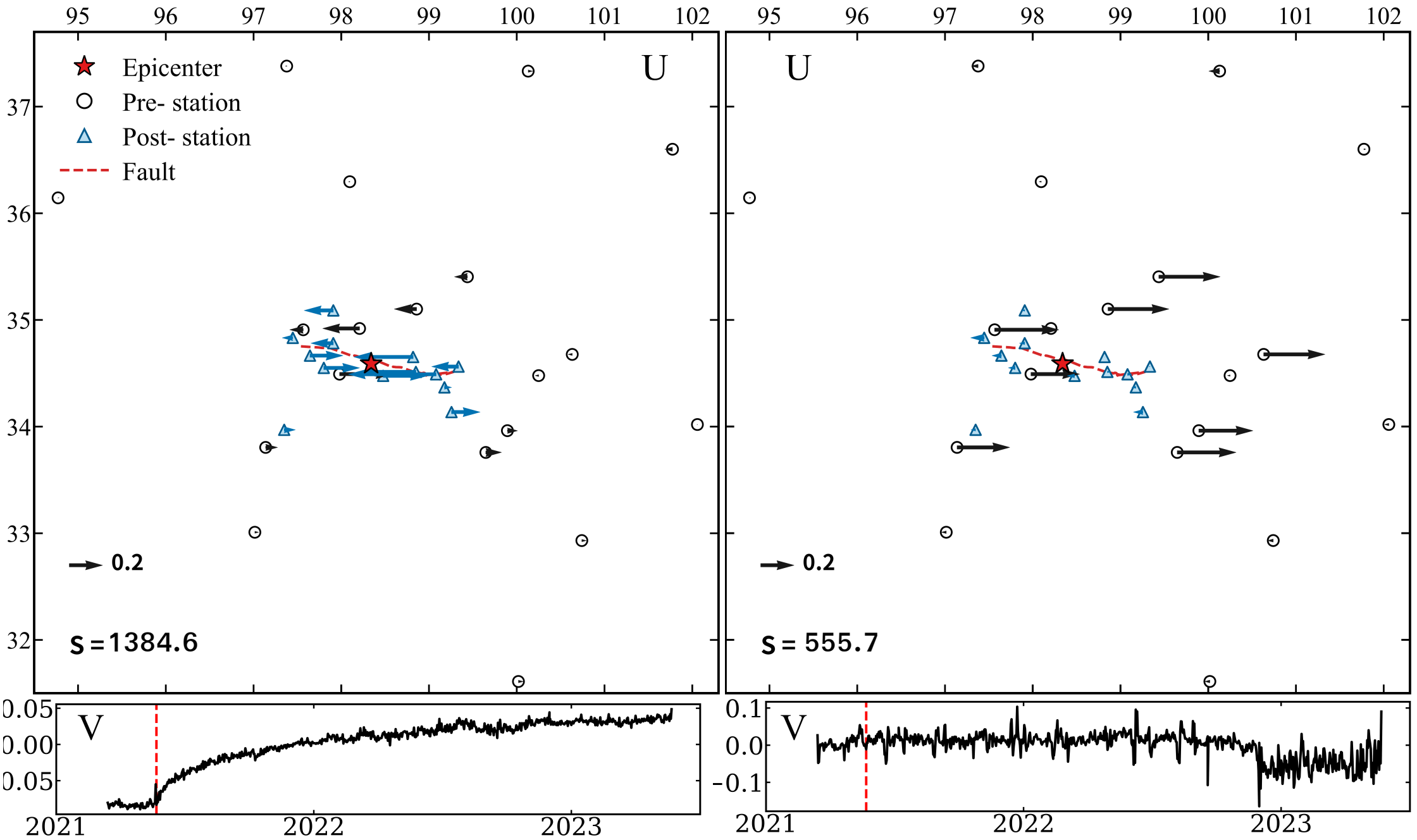
(a) First IC

(b) Second IC



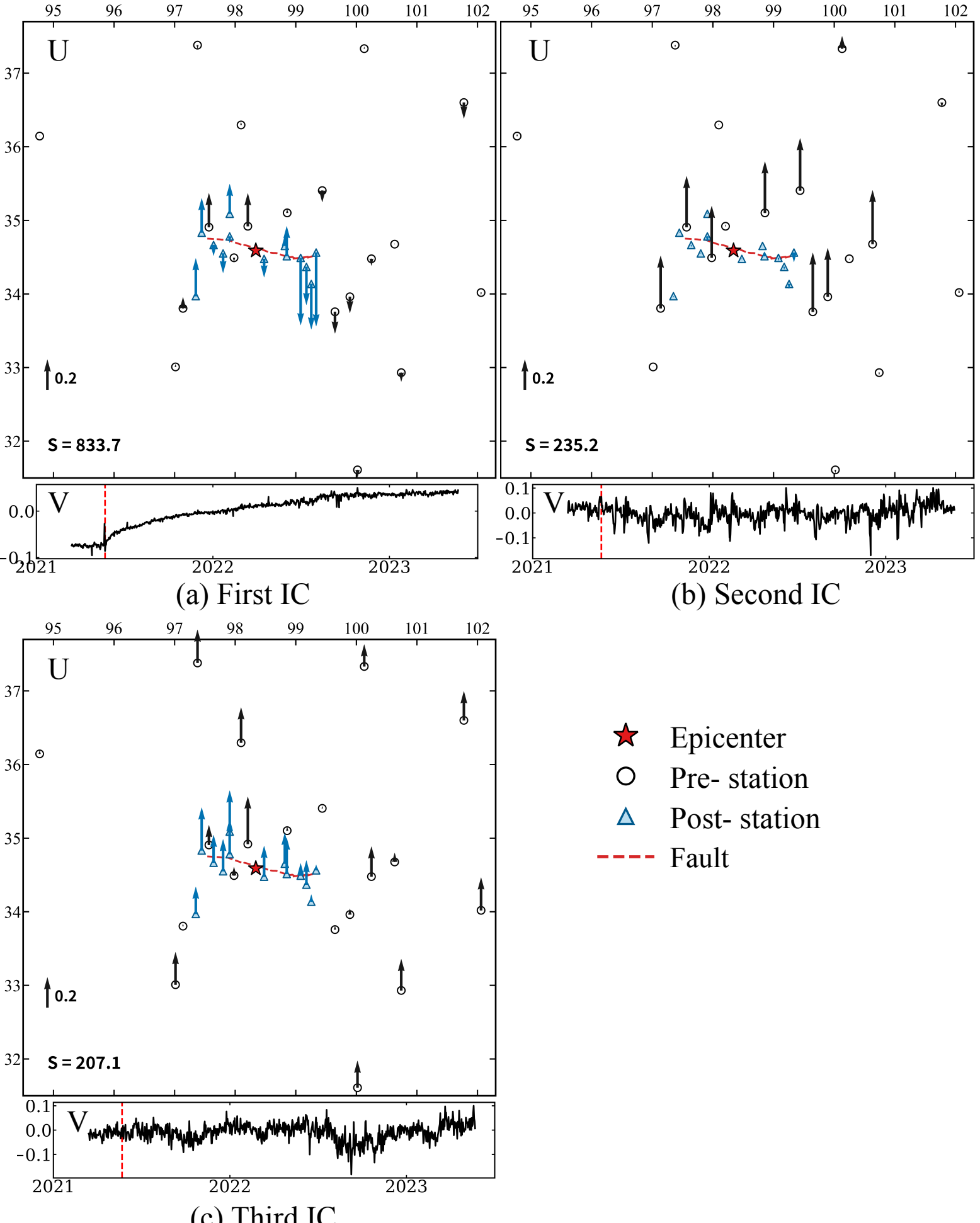
(a) First IC

(b) Second IC



(a) First IC

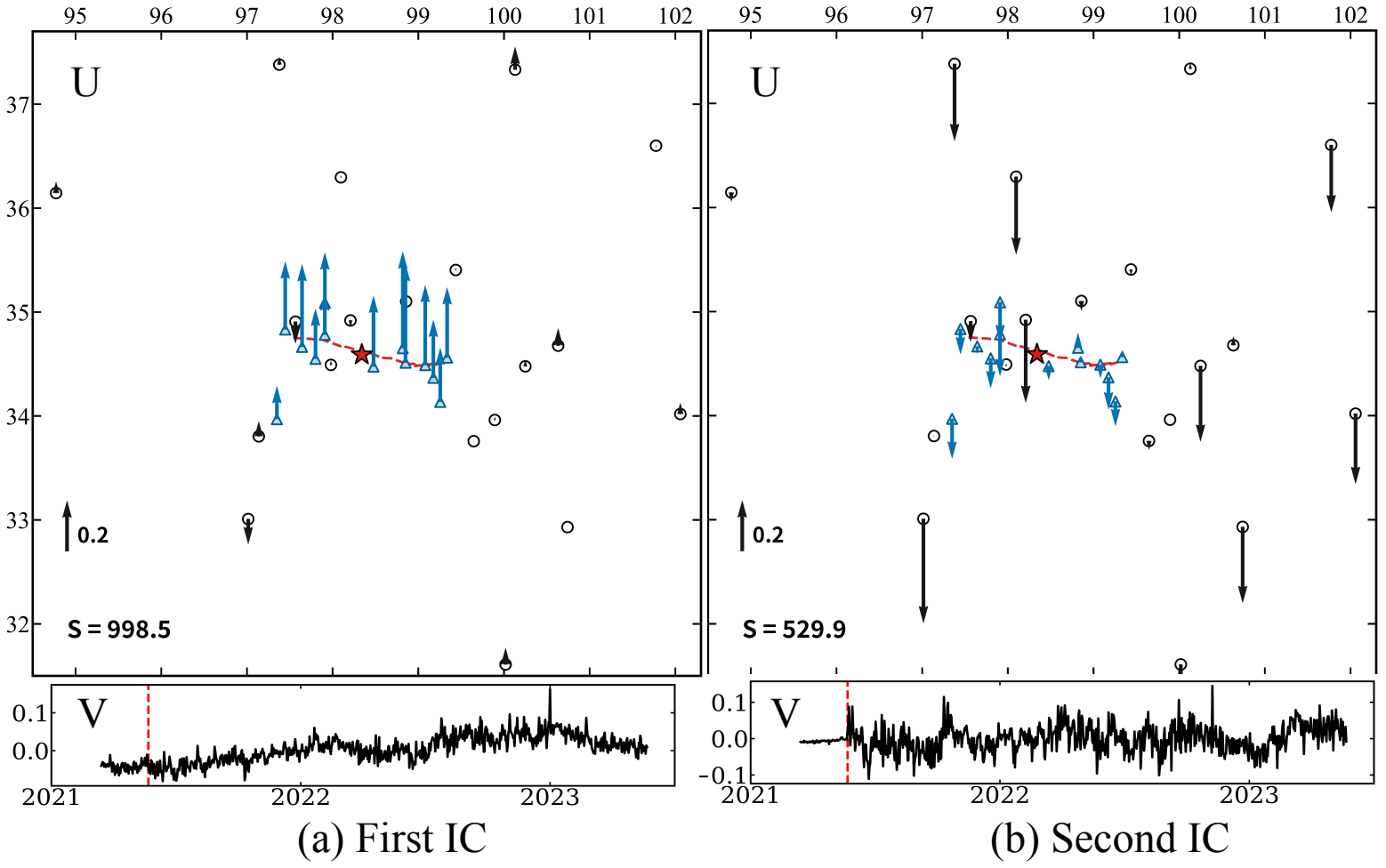
(b) Second IC



(a) First IC

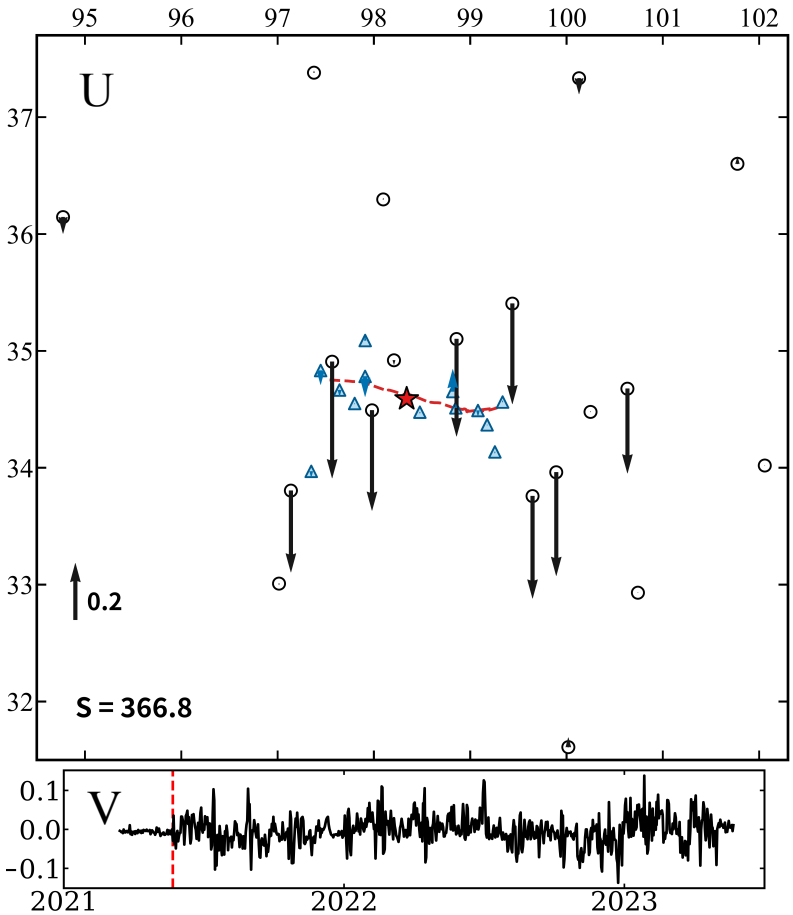
(b) Second IC

(c) Third IC

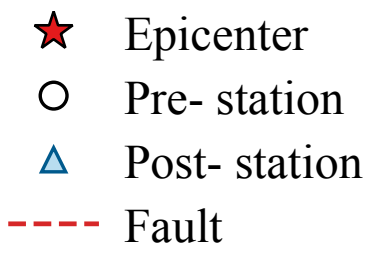


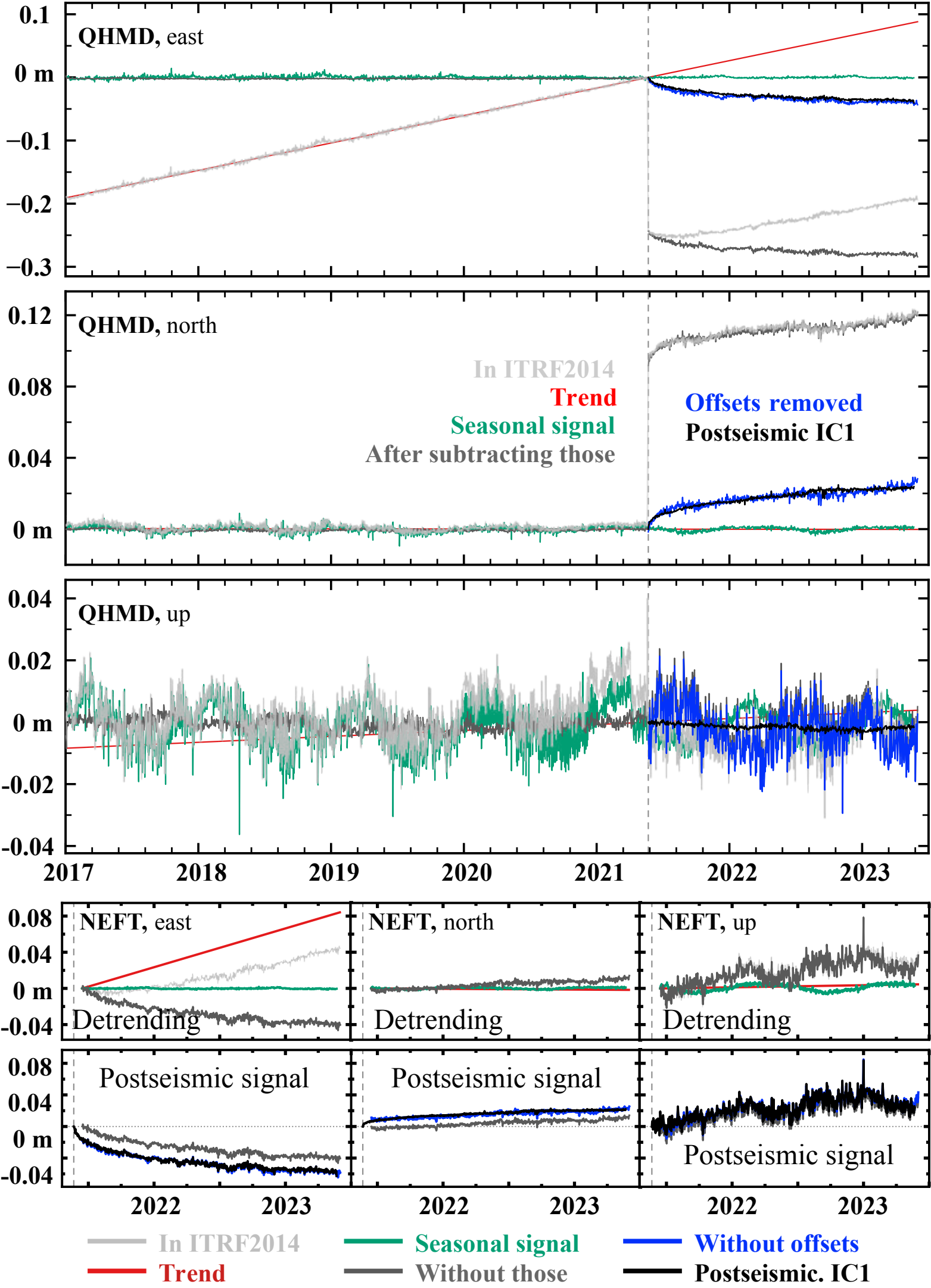
(a) First IC

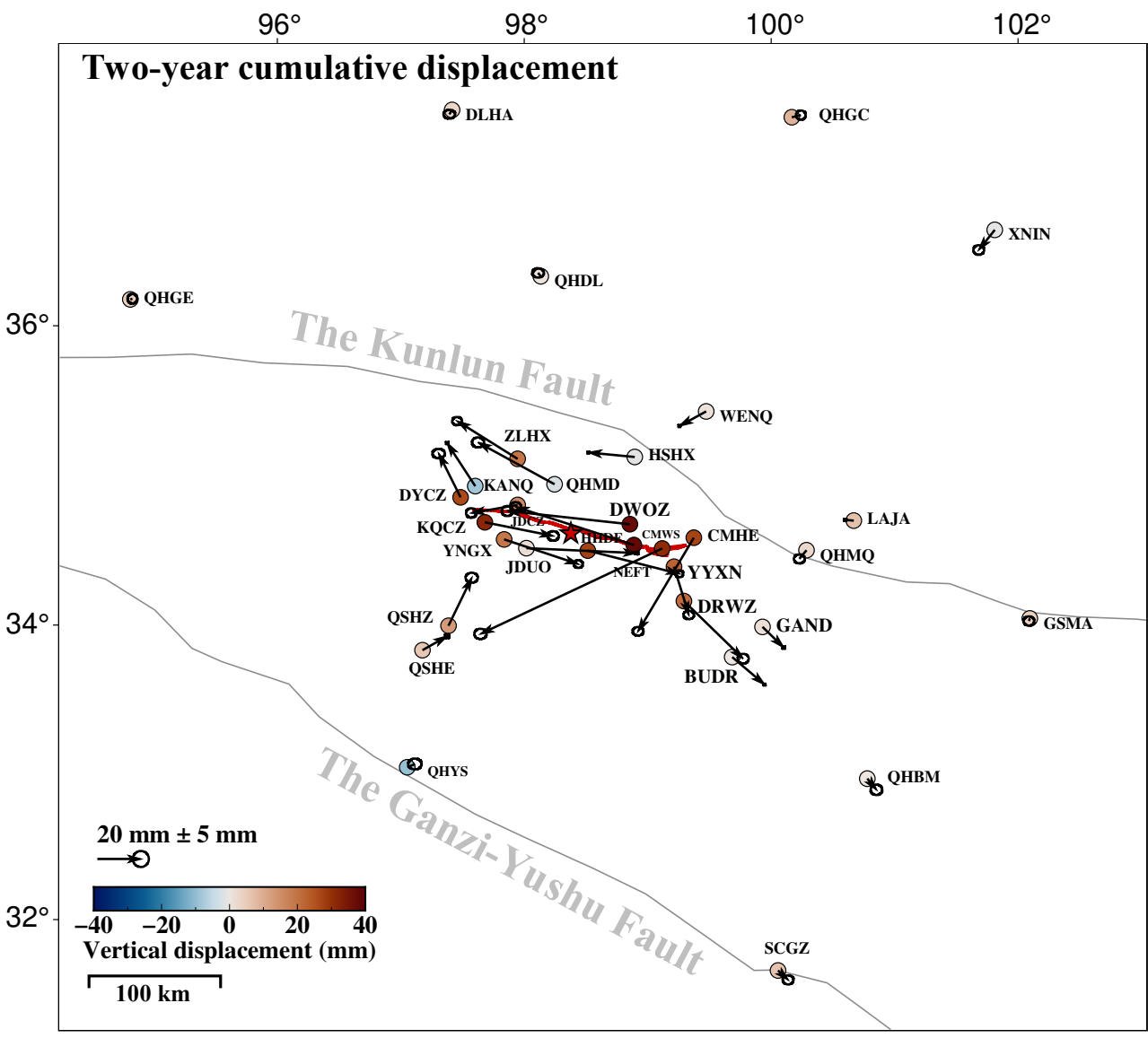
(b) Second IC

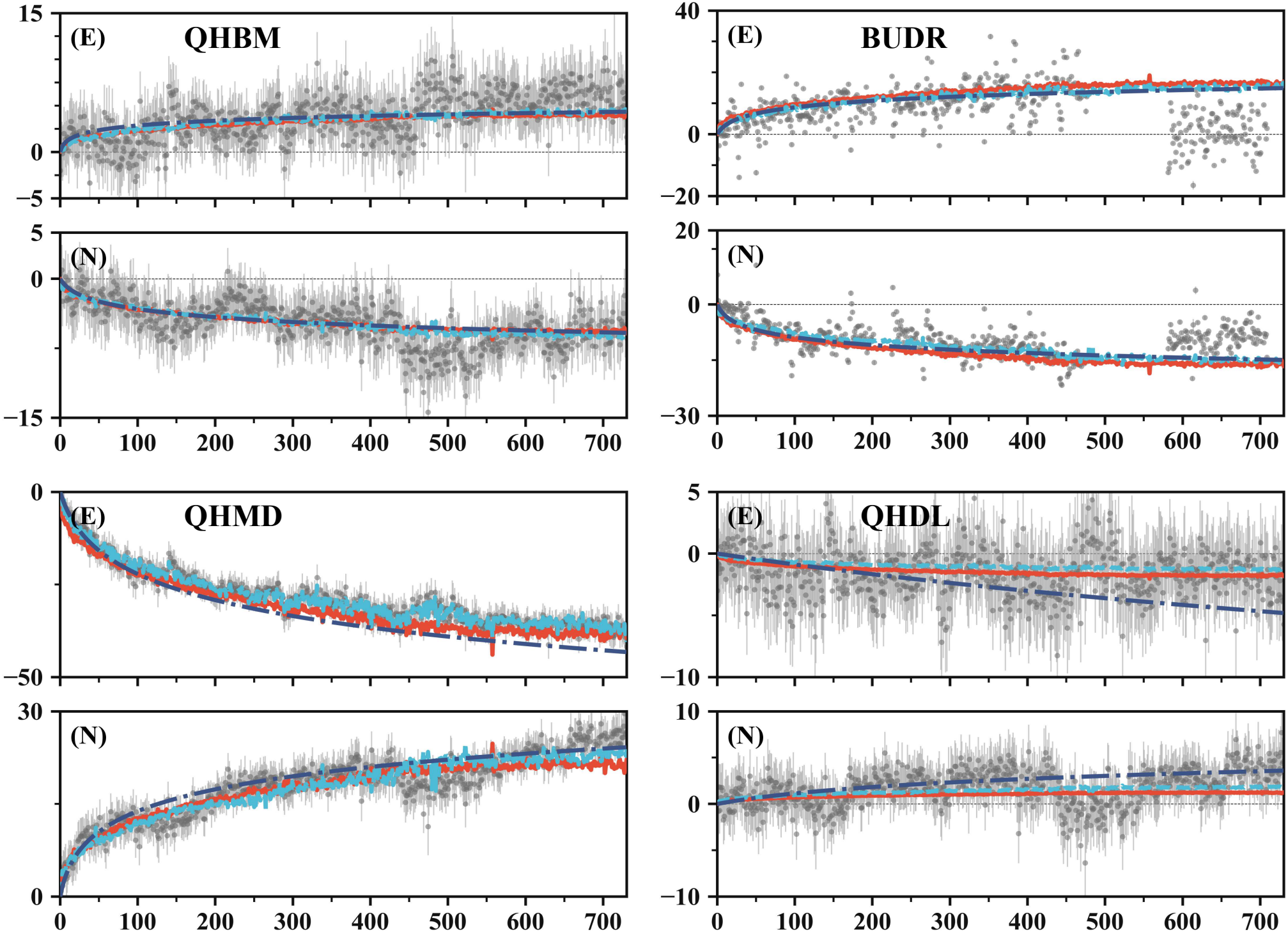


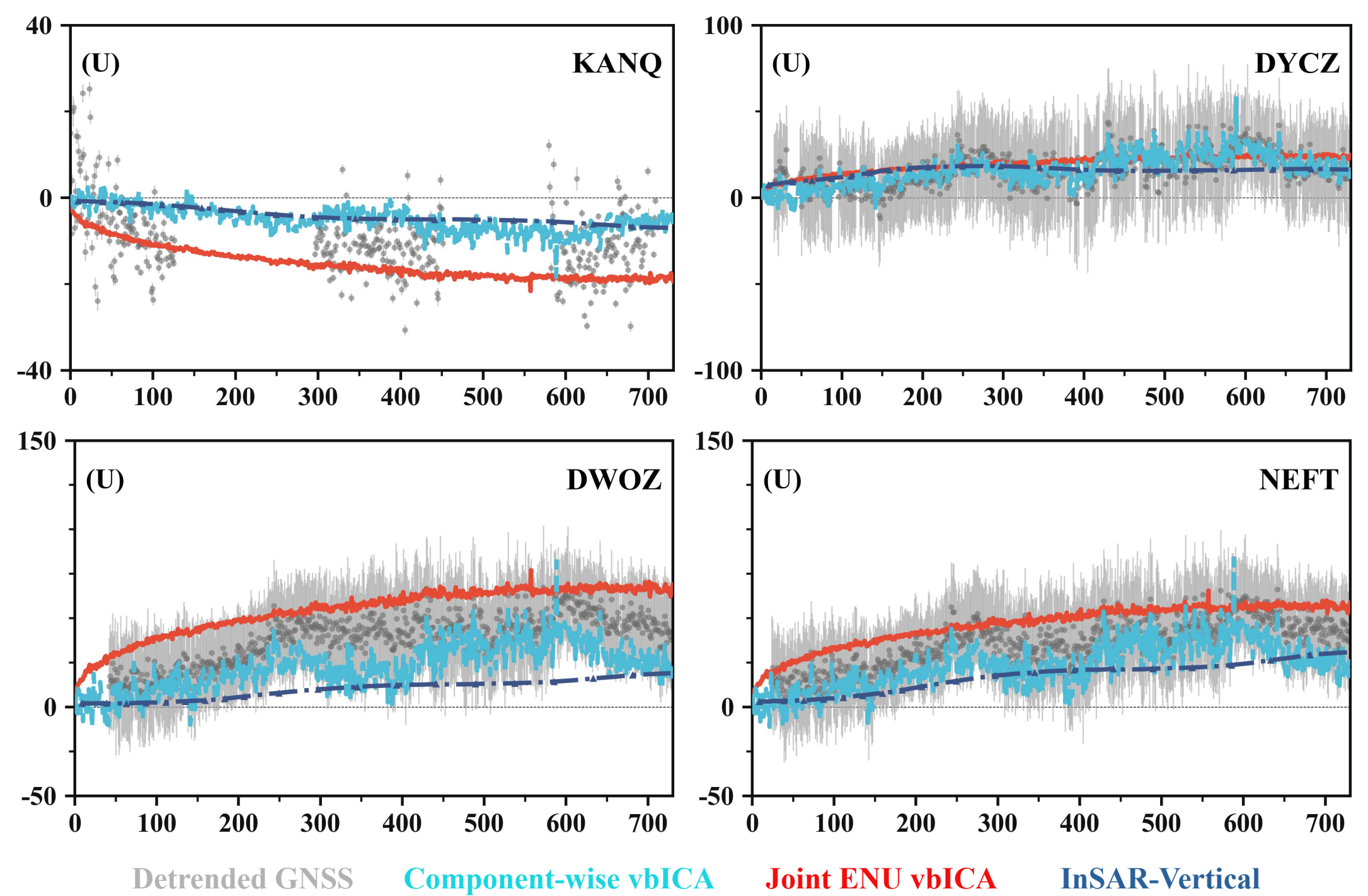
(c) Third IC




QHMD, east
QHMD, north
In ITRF2014
Trend
Seasonal signal
After subtracting those
Offsets removed
Postseismic IC1
QHMD, up
NEFT, east
NEFT, north
NEFT, up
Detrending
Detrending
Detrending
Postseismic signal
Postseismic signal
Postseismic signal
In ITRF2014
Trend
Seasonal signal
Without those
Without offsets
Postseismic. IC1


Two-year cumulative displacement
96°
98°
100°
102°
36°
34°
32°
DLHA
QHGC
XNIN
QHDL
QHGE
The Kunlun Fault
WENQ
ZLHX
HSHX
KANQ
QHMD
DYCZ
DWOZ
KQCZ
JDCZ
BHDE
CMWS
CMHE
LAJA
YNGX
JDUO
NEFT
YYXN
QHMQ
DRWZ
GAND
GSMA
QSHZ
QSHE
BUDR
QHYS
QHBM
The Ganzi-Yushu Fault
SCGZ
20 mm ± 5 mm
−40 −20 0 20 40
Vertical displacement (mm)
100 km


(E)
QHBM
(N)
(E)
BUDR
(N)
(E)
QHMD
(N)
(E)
QHDL
(N)
Detrended GNSS
Component-wise vbICA
Joint ENU vbICA
log fit (Xiong (2025))


(U)
KANQ
40
0
-40
0
100
200
300
400
500
600
700
(U)
DYCZ
100
0
-100
0
100
200
300
400
500
600
700
(U)
DWOZ
150
0
-50
0
100
200
300
400
500
600
700
(U)
NEFT
150
0
-50
0
100
200
300
400
500
600
700
Detrended GNSS
Component-wise vbICA
Joint ENU vbICA
InSAR-Vertical

Supplementary Files

This is a list of supplementary files associated with this preprint. Click to download.

- Graphicalabstract.png
- SI.docx